Available online at www.sciencedirect.com
SCIENCE DIRECT®
Journal of Computational Physics 209 (2005) 139–178
JOURNAL OF COMPUTATIONAL PHYSICS
www.elsevier.com/locate/jcp

A compressible flow model with capillary effects

Guillaume Perigaud [a], Richard Saurel [a,b,*]

[a] Polytech Marseille, UMR CNRS 6595 IUSTI, 5 rue E. Fermi, 13453 Marseille Cedex 13, France
[b] Institut Universitaire de France and INRIA Projet SMASH, 5 rue E. Fermi, 13453 Marseille Cedex 13, France

Received 22 December 2004; received in revised form 1 March 2005; accepted 17 March 2005
Available online 12 May 2005

Abstract

A quasi-conservative formulation for compressible flows with interfaces including both capillary and viscous effects is developed. The model involves: (i) acoustic and convective transport; (ii) surface tension effects introduced as an extension of the CSF method (Brackbill et al.) to compressible flows; (iii) viscous effects. The interfaces are considered as diffused zones. Every point of the flow is correctly described thanks to a mixture equation of state based on energy conservation and pressure equilibrium. The model is thus valid in each pure fluid as well as at interfaces. A Godunov type method, that enables interface capturing, is developed and used whatever the mesh point. Numerical tests are performed over a wide range of physical situations involving surface tension, compressibility, gravity, viscosity and large density ratios. Tests involving break-up and coalescence are considered to show the ability of the method to deal with dynamic appearance and disappearance of interfaces in an Eulerian framework.

Keywords: Two-phase flows; Interface capturing; Surface tension; Viscosity; Conservative formulation; Mixture thermodynamics; Compressibility; Break-up; Coalescence

1. Introduction

Flows with interfaces are part of our daily life. They are widespread, complex and very diverse. They are thus involved in many industrial processes from off-shore engineering to automotive (carburant injection [3,5]) and chemical engineering. Moreover, the interface is the area where complex physics may occur (surface tension, heat and mass transfers). So building of a model and a method to describe flows with interfaces seems of great interest from both theoretical and industrial point of view. Therefore, many

* Corresponding author.
E-mail addresses: guillaume.perigaud@polytech.univ-mrs.fr (G. Perigaud), richard.saurel@polytech.univ-mrs.fr (R. Saurel).

0021-9991/$ - see front matter © 2005 Elsevier Inc. All rights reserved.
doi:10.1016/j.jcp.2005.03.018

approaches have been developed to solve such problems both in an incompressible [23,25,41,57] and in a compressible [1,2,6,31,33,46] framework. Associated numerical methods consider that interfaces remain sharp while others handle smeared contact discontinuities.

The first type of numerical methods, we call "Sharp Interface Methods" (SIM), consists of four main families. The first widespread used techniques are the Lagrangian [7] and ALE (Arbitrary Lagrangian Eulerian) methods [16,26,50], where the interface is a coordinate line which evolves and deforms at the local flow velocity. They are the most natural methods which consider interfaces as true discontinuities. The second family corresponds to Front-Tracking methods. On the contrary of the preceding methods, front tracking procedures are performed on a fixed grid. They combine Eulerian solvers for flow far from interfaces and specific solvers closed to it. In spite of the hardness of the problem, methods, which are derived from this concept, give impressive results even in three dimensions [20]. The third family is the interface reconstruction techniques which are more widespread and quite easier to code [25]. In this case, interfaces are not exactly tracked, but are rebuilt thanks to the determination of advected phase volume fractions [23,42,43]. The fourth family consists of the Level Set methods [39], which combine front location and thermodynamic or extrapolation procedures to compute flow variables [41,51,52,62].

The second type of numerical methods, we call "Diffuse Interface Methods" (DIM) is essentially based on Eulerian formulations. On the contrary of SIM, DIM do not describe interfaces as discontinuities but as continuous zones where the transition from one medium to the other is quite smooth. Diffusing the interface implies that those methods create an artificial mixture zone close to the interface. The thermodynamic parameters in this mixture are thus unknown so that conventional thermodynamic treatment is no longer valid. In order to solve this problem, some authors have built Eulerian models for two-phase flows where the equations remain valid in pure fluids as well as at the interface. The equations are then solved by a single numerical procedure [1,2,38,45,40]. The challenge is to get consistent thermodynamic laws for the artificial mixture. To do this, some authors proposed to build governing equations for equation of state parameters [1,45]. This strategy has been retained and improved by Massoni et al. [38] and Allaire et al. [2]. In those references, the authors build a mixture equation of state which describes correctly pure fluids as well as artificial mixtures. In the mean time, other attempts to describe two-phase flows with several velocities have been developed. In [46], a method is proposed which is based on a two-phase flow model with seven equations, initially suggested in [6]. This method can be employed with various equations of state and in a wide range of physical applications such as flows with interfaces [46], cavitation and detonation waves [47]. One of its advantages relies on its ability to compute the creation and the evolution of the interfaces.

In this paper, we show the connection between two-phase flow mixture methods [6,46] where each fluid has its own velocity, pressure and density, and homogenous models with single pressure and velocity such as those presented in [2,38,40], thanks to an asymptotic analysis. Indeed, our goal is to introduce viscous effects and capillary ones into similar type of modelling. Thanks to the link between the two preceding different modelling approaches, viscous effects are easily introduced into the DIM, extending thus the model of these authors and reaching the first goal of the present modelling issues.

The second modelling issue corresponds to capillary effects in a compressible framework. Eulerian capillary-compressible flow models are present in the literature [11,29,30]. However, those models present some drawbacks for the applications we are here interested in. In these models, surface tension is a genuine characteristic of the fluids and an interface length scale, η, has to be set to correctly describe interfaces. This length scale η is usually very small ($\eta \simeq 10^{-8}$ m) so that it may lead to very difficult computational issues to get an accurate space and time interface resolution. Moreover, this approach is valid only when miscible fluids (liquid and its vapour) are present. At last, literature results show only low density ratios computations.

In the present article we are interested in compressible flows with interfaces separating non-miscible fluids such as air/water flows whose density ratio may be quite large. In order to succeed in modelling capillary

effects within a compressible two-phase flow framework, we extend the CSF method of Brackbill [8] to compressible fluids and embed it into the DIM family. It appears that the resulting model structure is very similar to second gradient theory models [11,29,30]. Nevertheless, major differences are to be noticed especially regarding thermodynamics and the interface length scale η, which is no longer present.

The next challenge is to numerically solve this model. It will be shown that the new model can be considered hyperbolic according that geometrical variables of the model (main curvature κ) are frozen with respect to flow variables. A specific hyperbolic solver is thus developed with an exact Riemann solver. The conservative formulation of the capillary model enables the derivation of an appropriate finite volume scheme including capillarity and dissipative effects. Boundary conditions are examined in particular wetting wall boundary conditions.

This article is thus organised as follows. In the first section, we derive the parent two-phase flow model with two-velocities. It is obtained by considering that each phase is separately governed by the Navier–Stokes equations. An averaging procedure is then applied onto the system to get the sought equations. This parent model involves pressure and velocity relaxation terms that control the rate at which mechanical equilibrium is reached. Assuming that those relaxation terms tend to infinity, an asymptotic analysis is performed to get the two-phase transport model with a single velocity including dissipative effects.

In the second section, capillary effects are modelled assuming inviscid fluids. The CSF method is used to include surface tension phenomena in the momentum equation. This approach is here extended to compressible framework by including surface tension energy contribution. A conservative formulation is then obtained.

In the third section, a mathematical study is addressed to the system including capillarity (eigenvectors and eigenvalues, hyperbolicity). Those ingredients are used to build a Godunov type scheme to compute conservative fluxes as well as volume fraction advection.

In the last section, a wide variety of physical situations are studied as numerical examples. Low speed flows (droplet break-up, rise of gas bubble) as well high speed flows (shocks, underwater explosions) are considered. First some analytical solutions are recovered: Laplace formula and deformed drop oscillations. Second, drop creation and breakup tests show the ability of the method to manage dynamic appearance and disappearance of free interfaces. Third, two-dimensional viscous liquid jet instabilities show that the method is able to deal with fluids with large density ratios. In the end, rise of gas bubbles in a liquid bulk, underwater explosion and drop collision tests show that the approach correctly treats problems with complex physics. These tests show very good agreement with experiments and analytical data.

2. Compressible flow model building

As mentioned earlier, interface problems in the context of Diffuse Interface Methods can be solved either by single pressure and velocity models [1,2,31,38,45] or two pressures and velocities two-phase flow models including relaxation [46,47]. This second type of models has some particular advantages that would be useful to keep. Here we propose a link between those approaches on the basis of an asymptotic analysis of the compressible multi-phase flow model (seven equations). This analysis follows the one of Kapila et al. [31] which was done in another context (granular materials) and the recent work of Murrone and Guillard [40]. It enables the extension of Massoni et al. [38] and Allaire et al. [2] models to viscous effects. Capillary effects are not considered hereafter. This issue will be addressed in Section 3.

2.1. The parent model with viscous effects

To obtain the parent compressible two-phase flow model we assume each phase k is governed by the Navier–Stokes equations. We then select the fluid k by multiplying the Navier–Stokes equations by the

characteristic function of phase k, χ_k ($\chi_k = 1$ when the point is in phase k and $\chi_k = 0$ otherwise). An averaging procedure, similar to that used by Drew [13,4], is then applied onto the system and leads to the final equations where some specific terms appear. Those terms express the interaction forces and work whose role is to drive the flow back to mechanical equilibrium. Assuming that the mixture is composed of phase k and phase k', the governing equations for phase k are thus:

$$\begin{cases} \dfrac{\partial \alpha_k}{\partial t} + \overrightarrow{u_I} \cdot \overrightarrow{\nabla \alpha_k} = \varpi\big((P_k - P_{k'}) + (P_{\mu_k} - P_{\mu_{k'}})\big), \\ \dfrac{\partial \alpha_k \rho_k}{\partial t} + \operatorname{div}(\alpha_k \rho_k \overrightarrow{u_k}) = 0, \\ \dfrac{\partial \alpha_k \rho_k \overrightarrow{u_k}}{\partial t} + \operatorname{div}(\alpha_k \rho_k \overrightarrow{u_k} \otimes \overrightarrow{u_k}) + \overrightarrow{\nabla(\alpha_k P_k)} = \overrightarrow{\operatorname{div}}(\alpha_k \bar{\bar{\tau}}_k) + P_I \overrightarrow{\nabla \alpha_k} - \bar{\bar{\tau}}_I \overrightarrow{\nabla \alpha_k} + \lambda\big(\overrightarrow{u_{k'}} - \overrightarrow{u_k}\big), \\ \dfrac{\partial \alpha_k E_k}{\partial t} + \operatorname{div}(\alpha_k (E_k + P_k) \overrightarrow{u_k}) = \operatorname{div}\big(\alpha_k \bar{\bar{\tau}}_k \cdot \overrightarrow{u_k}\big) + P_I \overrightarrow{u_I} \cdot \overrightarrow{\nabla \alpha_k} - \overrightarrow{u}_I \cdot \Big(\bar{\bar{\tau}}_I \cdot \overrightarrow{\nabla \alpha_k}\Big) \\ \qquad\qquad - \varpi \psi_I \big((P_k - P_{k'}) + (P_{\mu_k} - P_{\mu_{k'}})\big) + \lambda \overrightarrow{u_I}\big(\overrightarrow{u_{k'}} - \overrightarrow{u_k}\big) \end{cases} \tag{1}$$

with $\psi_I = P_I + P_{\mu_I}$. We note ρ_k, α_k, $\overrightarrow{u_k}$, P_k and ε_k the partial density, the volume fraction, the velocity vector, the pressure and the internal energy for each phase k respectively. The total energy, E_k, is defined as

$$E_k = \rho_k \varepsilon_k + \frac{1}{2} \rho_k \overrightarrow{u_k} \cdot \overrightarrow{u_k}.$$

$P_{k'}$ and $\overrightarrow{u_{k'}}$ are the variables of the other phase. P_I and $\overrightarrow{u_I}$ are called the average interface pressure and velocity. In the state of the art, several expressions are given for those quantities. For instance, in [6] P_I equals the gas pressure while $\overrightarrow{u_I}$ equals the condensed phase velocity:

$$\begin{cases} P_I = P_{k'}, \\ \overrightarrow{u}_I = \overrightarrow{u}_k. \end{cases} \tag{2}$$

It is useful to note that the symmetric option:

$$\begin{cases} P_I = P_k, \\ \overrightarrow{u}_I = \overrightarrow{u}_{k'} \end{cases} \tag{3}$$

is possible as well. More sophisticated estimates have recently been proposed [48,4]:

$$\begin{cases} P_I = \dfrac{Z_k P_{k'} + Z_{k'} P_k}{Z_k + Z_{k'}} + \operatorname{sign}\left(\dfrac{\partial \alpha_k}{\partial x}\right) \dfrac{(u_{k'} - u_k) Z_k Z_{k'}}{Z_k + Z_{k'}}, \\ u_I = \dfrac{Z_k u_k + Z_{k'} u_{k'}}{Z_k + Z_{k'}} + \operatorname{sign}\left(\dfrac{\partial \alpha_k}{\partial x}\right) \dfrac{P_{k'} - P_k}{Z_k + Z_{k'}}, \end{cases} \tag{4}$$

where Z represents the acoustic impedance ($Z = \rho c$).

Nevertheless, the choice of P_I and $\overrightarrow{u}_I$ has no consequences onto the asymptotic analysis since the expansions are made closed to an equilibrium state where all pressures and velocities are equal. The simplest analytical guess (2) is thus retained to perform the following analysis.

The term P_{μ_k} strongly depends on the problem under study. It represents the integration of viscous stresses over the interfaces, which are present into a two-phase control volume. In order to simplify such a calculation, we impose a structure to the mixture: we assume that the microscopic mixture between liquid and gas is made of small spherical inclusions (bubbles or drops). In this case, the viscous "pressure" P_{μ_k} reads, following [48],

$$P_{\mu_k} = \frac{4}{3} \mu_k \frac{\dot{\alpha}_k \alpha_{k'}}{\alpha_k},$$

where μ_k represents the dynamic viscosity of phase k and $\dot{\alpha}_k$ $(= \varpi\Delta(P + P_\mu))$ the volume fraction variation (the right-hand side of the first equation of system (1).

Thus system (1) is able to model non-equilibrium two-phase mixtures in the presence of viscous effects. We note the presence of pressure and velocity relaxation terms, $\lambda\Delta\overrightarrow{u}$ and $\varpi\Delta(P + P_\mu)$, which drive the system back to mechanical equilibrium. The relaxation parameters λ and ϖ control the rate at which this equilibrium is reached.

This set of equations is very similar to a rather general model developed by Baer and Nunziato [6]. It has first been used to compute detonation waves in granular mixtures. More recently Saurel and Abgrall [46] have used its formalism to solve interface problems as well as cavitation in liquids [47] (see also the non-equilibrium approach of Le Metayer et al. [34]), or mixtures of turbulent fluids [48].

2.2. Asymptotic analysis of the parent multi-phase flow model with stiff relaxation

Relaxation terms drive the system back to mechanical equilibrium. To describe flows with interfaces, jumps conditions across the contact discontinuity must be fulfilled. Such a goal can be reached by imposing instantaneous pressure and velocity equilibrium [46]. In their numerical algorithm the authors use a procedure where λ and ϖ tend to infinity such that pressures and velocities in both phases relax toward an equilibrium state at any time. The limit model corresponding to such a relaxation procedure seems of great interest for the modelling of flows with interfaces. Such a model is determined by the analysis summarised hereafter, following the lines of Kapila et al. [31].

We thus determine the limit system by asymptotic reduction of system (1), where viscous effects are accounted for, as λ and ϖ tend to infinity. Phases are denoted by subscripts 1 and 2. Moreover, we recall that: $P_I = P_2$, $\psi_I = \psi_2$, $\overrightarrow{u}_I = \overrightarrow{u_1}$. In order to carry out the asymptotic analysis, λ and ϖ are written in the following form:

$$\lambda = \frac{1}{\varepsilon} \quad \text{and} \quad \varpi = \frac{1}{\varepsilon} \qquad \text{where } \varepsilon \to 0^+.$$

The two-phase flow model (1) can be written in the general form under primitive variable U:

$$\frac{\partial U}{\partial t} = F(U) + \frac{1}{\varepsilon}\Psi(U),$$

where

$$U = \begin{pmatrix} \alpha_1 \\ \alpha_1\rho_1 \\ \overrightarrow{u_1} \\ P_1 \\ \alpha_2\rho_2 \\ \overrightarrow{u_2} \\ P_2 \end{pmatrix} \quad \text{and} \quad \Psi(U) = \begin{pmatrix} P_1 - P_2 + P_{\mu_1} - P_{\mu_2} \\ 0 \\ \overrightarrow{u_2} - \overrightarrow{u_1} \\ -(\psi_2 - \rho_1^2 K_1)(P_1 - P_2 + P_{\mu_1} - P_{\mu_2}) \\ 0 \\ -(\overrightarrow{u_2} - \overrightarrow{u_1}) \\ (\psi_2 - \rho_2^2 K_2)(P_1 - P_2 + P_{\mu_1} - P_{\mu_2}) - \|\overrightarrow{u_2} - \overrightarrow{u_1}\|^2 \end{pmatrix}.$$

F and Ψ are regular enough functions close to the mechanical equilibrium state, U_o, to allow a Taylor expansion. F depends on U but also on U-space derivatives. Assuming state U can be expressed as a sum of a constant state with respect to ε and a small fluctuation of order ε and of magnitude U_1 we get

$$U^\varepsilon = U_o + \varepsilon U_1.$$

Thus we obtain on one hand,

$$F(U^\varepsilon) = F(U_o) + \varepsilon \frac{\partial F(U)}{\partial U}(U_o)U_1$$

and on the other hand

$$\Psi(U^\varepsilon) = \Psi(U_o) + \varepsilon \frac{\partial \Psi(U)}{\partial U}(U_o)U_1.$$

Those equations become as asymptotic analysis is carried out:

(i) At $\frac{1}{\varepsilon}$ order, we get a necessary condition for the system to be consistent:

$$\forall \varepsilon > 0 \quad \frac{\Psi(U_o)}{\varepsilon} = 0 \quad \text{which is equivalent to} \quad \Psi(U_o) = 0.$$

(ii) At 0 order, we get the first form of the reduced model for flows with interfaces:

$$\frac{\partial U_o}{\partial t} = F(U_o) + \frac{\partial \Psi}{\partial U}(U_o)U_1.$$

2.3. Reduced model including viscous effects

The condition $\Psi(U_o) = 0$ applied to the general multi-phase flow model (1) show that velocities and pressures are equal at zero order. The pressure equilibrium is due to the fact that the 'viscous pressures' P_{μ_1} and P_{μ_2} vanish at zero order because $\dot{\alpha}_k$ is zero when equilibrium is reached. The limit of this model when relaxation coefficients tend to infinity gives the reduced model we were seeking. Indeed, after some calculation and keeping in mind that P_1, P_2 and $\overrightarrow{u_1}$, $\overrightarrow{u_2}$ are in equilibrium, we get the following system:

$$\begin{cases} \dfrac{\partial \alpha_1}{\partial t} + \overrightarrow{u} \cdot \overrightarrow{\nabla \alpha_1} - K \operatorname{div}(\overrightarrow{u}) = 0, \\ \dfrac{\partial \alpha_1 \rho_1}{\partial t} + \operatorname{div}(\alpha_1 \rho_1 \overrightarrow{u}) = 0, \\ \dfrac{\partial \alpha_2 \rho_2}{\partial t} + \operatorname{div}(\alpha_2 \rho_2 \overrightarrow{u}) = 0, \\ \dfrac{\partial \rho \overrightarrow{u}}{\partial t} + \operatorname{div}(\rho \overrightarrow{u} \otimes \overrightarrow{u}) + \overrightarrow{\nabla P} = \overrightarrow{\operatorname{div}}(\mu \bar{\bar{\tau}}), \\ \dfrac{\partial E}{\partial t} + \operatorname{div}((E+P)\overrightarrow{u}) = \operatorname{div}\left(\mu \bar{\bar{\tau}} \cdot \overrightarrow{u}\right), \end{cases} \tag{5}$$

where $K = (\rho_2 c_2^2 - \rho_1 c_1^2)/((\rho_1 c_1^2/\alpha_1) + (\rho_2 c_2^2/\alpha_2)) = \alpha_1 \alpha_2 (\rho_2 c_2^2 - \rho_1 c_1^2)/(\alpha_1 \rho_2 c_2^2 + \alpha_2 \rho_1 c_1^2)$ and subscript "o" has been omitted for the sake of clarity.

α_1 denotes the gas volume fraction, α, so we have $\alpha_2 = (1 - \alpha)$, while ρ_1 and ρ_2 are the densities of phase 1 and 2. $\overrightarrow{u}$, P and E respectively represent the mixture velocity, pressure and total energy. The dissipative terms are accounted for by a viscous stress tensor, $\mu \bar{\bar{\tau}}$ where μ is a mixture dynamic viscosity. Their expressions are

$$\mu = \alpha_1 \mu_1 + \alpha_2 \mu_2, \tag{6}$$

$$\bar{\bar{\tau}} = -\frac{2}{3} \operatorname{div}(\overrightarrow{u}) \bar{\bar{I}} + 2 \bar{\bar{D}}, \tag{7}$$

where $\bar{\bar{D}} = \frac{1}{2}\left(\overline{\overline{\operatorname{grad}}}\,\overrightarrow{u} + (\overline{\overline{\operatorname{grad}}}\,\overrightarrow{u})^t\right)$ is the deformation rate tensor. The mixture density ρ is defined as $\rho = \alpha_1 \rho_1 + \alpha_2 \rho_2$ and is a conserved variable. This model contains nice features for the modelling of interface

problems. It naturally involves mechanical equilibrium between phases at any time which corresponds in fact to the interface conditions when the normal velocities and pressures are equal. Another remark is related to the acoustic properties of this model. The mixture speed of sound, c, for this model reads

$$\frac{1}{\rho c^2} = \frac{\alpha_1}{\rho_1 c_1^2} + \frac{\alpha_2}{\rho_2 c_2^2},$$

where

$$c_k^2 = \frac{\frac{P_k}{\rho_k^2} - \frac{\partial \varepsilon_k}{\partial \rho_k}\Big)_{P_k}}{\frac{\partial \varepsilon_k}{\partial P_k}\Big)_{\rho_k}}$$

is the speed of sound in phase k. The mixture speed of sound, c is known as Woods' relation [58,31]. This relation is in good agreement with experimental speed of sound measurements in liquid/gas mixtures. The system is hyperbolic as long as the equation of state for each phase is convex. It possesses two entropies, which are those of the general multi-phase flow model. They remain constant along streamlines. The preceding model (5), in absence of viscosity, has initially been derived by Kapila et al. in a different context. The authors were seeking a reduced multi-phase model for dense mixtures of packed powder beds in which drag and pressure relaxation effects are very fast [31]. Indeed, we have here recovered the same model where granular-contact pressure and contact energy have been removed while viscous effects have been included to model flow with interfaces. The volume fraction equation involves a velocity divergence term $K\,\mathrm{div}(\overrightarrow{u})$. This term implies gas volume fraction increase across rarefaction waves and decrease across compression ones. This is in agreement with the dynamics of an isolated bubble [19]. However, as we are interested in two-phase flows between pure fluids, simplifications can be done.

2.4. The hydrodynamic model for interfaces

While the preceding model describes fluid mixtures, our aim is to model interfaces separating pure fluids. Working with the previous model has some drawbacks: first the gas volume fraction positivity is not ensured by the model; and second, the shocks jump conditions is an issue [31]. Using it would lead to a useless complexity with regard to the problems we are here interested in (interface flows).

We are looking for a model that tends to the Navier–Stokes equations in each pure fluid and that realise their coupling across interfaces, so that we impose the gas volume fraction α not to vary across acoustic waves. We can then neglect $K\,\mathrm{div}(\overrightarrow{u})$ and obtain a simplified model which theoretically ensures gas volume fraction positivity. At this point, the model is no longer a mixture model, but is valid only for interface problems. The model including viscous effects now reads

$$\begin{cases} \dfrac{\partial \alpha_1}{\partial t} + \overrightarrow{u} \cdot \overrightarrow{\nabla \alpha_1} = 0, \\ \dfrac{\partial \alpha_1 \rho_1}{\partial t} + \mathrm{div}(\alpha_1 \rho_1 \overrightarrow{u}) = 0, \\ \dfrac{\partial \alpha_2 \rho_2}{\partial t} + \mathrm{div}(\alpha_2 \rho_2 \overrightarrow{u}) = 0, \\ \dfrac{\partial \rho \overrightarrow{u}}{\partial t} + \mathrm{div}(\rho \overrightarrow{u} \otimes \overrightarrow{u}) + \overrightarrow{\nabla P} + \overrightarrow{\mathrm{div}}(\mu \bar{\bar{\tau}}) = 0, \\ \dfrac{\partial E}{\partial t} + \mathrm{div}((E+P)\overrightarrow{u}) + \mathrm{div}\big(\mu \bar{\bar{\tau}}.\overrightarrow{u}\big) = 0. \end{cases} \tag{8}$$

The same simplification was done in the models of Massoni et al. [38] and Allaire et al. [2] in absence of viscosity. The corresponding models, very closed to system (8) have shown their hability to provide reliable results.

Before examining model's basic physical and mathematical properties (hyperbolicity, speed of sound, entropy existence) let us provide the thermodynamic closure of the two preceding models.

2.5. Thermodynamic closure

Our aim with those models is to deal with artificial mixture zones. Indeed, in the context of Eulerian methods, the numerical diffusion of contact discontinuities creates artificial mixtures. But as we have previously mentioned, the thermodynamic parameters of the cells in the smeared interface zone are unknown. Nevertheless, their knowledge is mandatory for the interface pressure computation, unless any compressible Eulerian method fails at the second time step [1,33,45]. The construction of a mixture equation of state (EOS) is the cure to such a problem. Indeed, such an EOS must be able to describe the flow whatever the location in the material, i.e. both in pure fluids and mixture zones. So, we first choose an EOS to describe each pure fluid; second, we use those EOS to build the mixture EOS.

As our applications only involve liquid and gas, we use the Stiffened Gas EOS [22,24] to describe the thermodynamics of those pure substances:

$$P_k = (\gamma_k - 1)\rho_k \varepsilon_k - \gamma_k P_{\infty_k}. \tag{9}$$

γ_k and P_{∞_k} are characteristic of the material. The terms associated to those parameters represent respectively repulsive and attractive molecular effects. Those parameters (γ_k, P_{∞_k}) can be determined by asymptotic expansion over experimentally determined reference curves (Hugoniot and saturation curves). A detailed procedure is proposed in [34]. The Stiffened Gas EOS has thus a wide range of validity. This EOS is convex so that $c_k^2 = -(\partial \varepsilon_k/\partial s_k)_{\rho_k}$ remains positive. The associated speed of sound can be easily expressed as $c_k = \sqrt{\gamma_k \frac{P_k + P_{\infty k}}{\rho_k}}$. In Table 1, thermodynamic data are gathered for several media at standard state. As a consequence of this formulation, the mixture EOS will be also of Stiffened Gas type. Indeed, we proceed as in [38] and [2] to build the required EOS. An isobaric closure is chosen, which is fully consistent with the assumptions made during the asymptotic analysis (pressure equilibrium). The mixture internal energy definition reads

$$\rho\varepsilon = \alpha_1\rho_1\varepsilon_1 + \alpha_2\rho_2\varepsilon_2.$$

By replacing each product $\rho_k\varepsilon_k$ by a function of pressure with the help of Eq. (9) and by using the isobaric closure, the mixture EOS reads

$$P = (\gamma - 1)\rho\varepsilon - \gamma P_\infty, \tag{10}$$

where the mixture EOS parameters γ and P_∞ are given by

$$\frac{1}{\gamma - 1} = \sum_k \frac{\alpha_k}{\gamma_k - 1} \quad \text{and} \quad \gamma P_\infty = \frac{\sum_k \frac{\alpha_k \gamma_k P_{\infty k}}{\gamma_k - 1}}{\sum_k \frac{\alpha_k}{\gamma_k - 1}}.$$

Table 1
Thermodynamic Stiffened Gas EOS parameters for several materials

	γ	P_∞ (Pa)	c (m/s)
Air	1.4	0	374
Water (atm. pres.)	4.1	4.4×10^8	1647
Water (high pres.)	4	6×10^8	1820
Copper	4.22	32.4×10^9	3910
Granite	2.6	14.2×10^9	3750

The mixture EOS enables the interface conditions to be fulfilled at any time. It is now important to scan some of the main properties of the model.

2.6. Properties of the simplified five equation model

In absence of viscous effects, this model corresponds to the ones presented in [38] and [2]. Note also that model (8) is a generalisation of the models given in [1,49,45]. Indeed, in the particular case of ideal gases, the mixture EOS reads

$$P = \frac{\rho\varepsilon}{\frac{\alpha_1}{\gamma_1-1}+\frac{\alpha_2}{\gamma_2-1}}.$$

The mixture polytropic coefficient then reads

$$\frac{1}{\gamma-1} = \frac{\alpha_1}{\gamma_1-1} + \frac{\alpha_2}{\gamma_2-1}$$

Since $\alpha_2 = 1 - \alpha_1$, and γ_1, γ_2 are constants, we deduce

$$\frac{\mathrm{d}\alpha_1}{\mathrm{d}t} = 0 \quad \text{is equivalent to} \quad \frac{\mathrm{d}}{\mathrm{d}t}\left(\frac{1}{\gamma-1}\right) = 0.$$

This evolution equation on the polytropic parameter is the key point of the numerical approaches developed in the preceding references, but it was restricted to ideal or "stiffened" gases only. As shown in [38], inaccuracies in the temperature computation were obtained. The present model does not suffer from these drawbacks [38,2].

Note also that the Riemann problem structure is quite similar to the one of the Euler equations. The reduced model has three eigenvalues $\lambda_1 = u - c$, $\lambda_2 = u$ and $\lambda_3 = u + c$ where c denotes the mixture speed of sound. Compared to the model where $K\,\mathrm{div}(\overrightarrow{u})$ was accounted for, the mixture speed of sound has now a different behaviour. The quantity ρc^2 may be expressed as a sum of $\rho_k c_k^2$ weighted by β_k functions:

$$\rho c^2 = \sum_k \beta_k \rho_k c_k^2 \quad \text{where } \beta_k = \frac{\frac{\alpha_k}{\gamma_k-1}}{\sum_j \frac{\alpha_j}{\gamma_j-1}}.$$

It may be written in compact form:

$$\rho c^2 = \gamma(P + P_\infty).$$

Functions β_k remain positive whatever the behaviour of α_k. It is then easy to conclude that ρc^2 is no longer an harmonic average of $\rho_k c_k^2$ as for Wood's formula but is a convex average of those quantities. The speeds of sound for models (5) and (8) are now compared in the Fig. 1. The behaviour of model (5) is in better agreement with experimental observations when dealing with physical fluid mixtures (bubbly flows for instance). However, when dealing with artificial mixtures, the use of model (5) may yield the computation failure. The speed of sound would be so low inside the numerical diffusion zone at interfaces that sonic points may occur without any flow acceleration, yielding very difficult approximation of Riemann invariants as well as Riemann solvers convergence. With model (8) the speed of sound does not imply such drawbacks. Moreover, with the mixture Stiffened Gas EOS, a mixture entropy, s, and a phase entropy for each fluid, s_k, may be found explicitly:

$$s_k = \frac{P + P_\infty}{\rho_k^\gamma} \quad \text{and} \quad s = Y_1 s_1 + Y_2 s_2,$$

where Y_1 and Y_2 are the mass fractions.

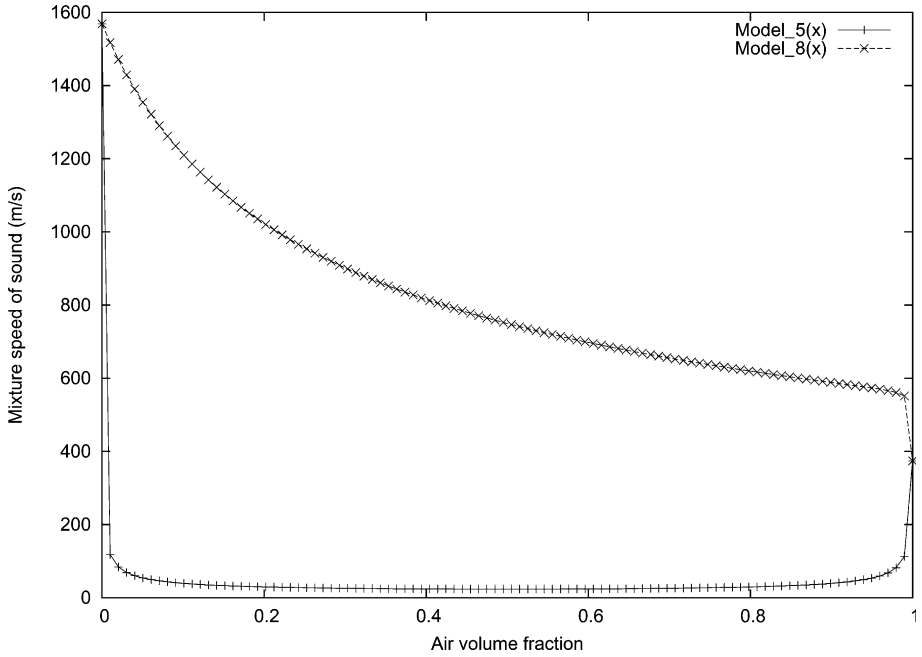

Fig. 1. Comparison of the speeds of sound for both reduced models (5) and (8).

They obey the following evolution equations:

$$\frac{\mathrm{d}s_k}{\mathrm{d}t} = 0 \quad \text{and} \quad \frac{\mathrm{d}s}{\mathrm{d}t} = 0.$$

Riemann invariants across rarefaction or compression waves can be analytically integrated [2]. An exact Riemann solver can thus be built. The exhibited model involves compressibility of each phase and presents nice mathematical properties. We do not deepen here the analysis since we are interested in the final model, which must include capillary effects. We now focus on such an extension.

3. A compressible two-phase flow model with surface tension effects

In some specific situations, even if the flow velocity is low enough to consider the flow as incompressible, volume, density or temperature variations are such that a compressible approach is needed to fit the physical problem. Evaporation phenomena, cryogenics, cavitation and bubble collapse near a solid wall are examples where compressibility plays a major role. For such phenomena, surface tension may also have strong implications. Moreover growth of interface instabilities such as Rayleigh–Taylor or Kelvin–Helmholtz instabilities for instance, can be inhibited by surface tension effects. Indeed surface tension stabilizes the interface because it smoothes any of its small disturbances. Up to our knowledge, surface tension effects are computed within the incompressible framework whereas compressibility effects are either neglected or poorly considered. Therefore a compressible model including surface tension effects would be useful. The following paragraphs thus present the modelling of capillary effects within the compressible framework of system (8). These developments are done in absence of viscosity.

3.1. Conventional modelling

Most of physical problems that involve surface tension are considered in an incompressible framework, where the interface is treated as a true mathematical discontinuity. Surface tension forces and local curvature are determined easily as soon as the interface is accurately located [20,25,52,23].

Nevertheless, all incompressible algorithms do not describe interfaces without diffusion. The topic of diffuse interfaces is precisely the context in which Brackbill et al. [8] proposed to model capillary effects. The CSF (Continuum Surface Force) method has shown its efficiency and is widespread in the area of incompressible flows [23,42,43,61].

On the contrary very few attempts for compressible flows can be noticed. In [29] and [30] a thermodynamic framework based on Cahn–Hilliard model [11] was proposed. According to that theory, internal energy is not a function of flow variables only but also of their derivatives. Such mixtures are thus characterised by a parameter λ called inner tension coefficient. To compute physical surface tension driven problems one has to set an interface thickness η in order to get the physical surface tension coefficient between fluids, σ, by integrating the quantity $\lambda|\nabla\psi|^2$ over the length η, where ψ is a so called order parameter. The numerical resolution requires spatial resolution of the interface too and thus may lead to computational issues. This theory has been developed especially for water/steam binary mixtures where density ratios remain low (less than 5) even if some recent attempts to extend such a formalism to flows far from the critical point [30] are to mention.

Such models were initially derived to deal with capillary effects, compressibility and phase transition across interfaces. They are built on the basis of a mixture equation of state for a liquid and its vapour. Their extension to interfaces separating non-miscible fluids is not obvious, in particular because of the thermodynamic closure which consider one temperature and entropy only. Indeed an interface separating fluids is precisely a location of equal pressures and velocities, but different temperatures, densities and entropies. As shown in [38], the here presented model involves two temperatures. Also, it does not contain any length scale regarding the interface. It is considered as an artificial diffusion zone whose thickness depends only on the numerical scheme and cell size. Moreover, there is no limitation regarding the density ratio. We will show applications involving density ratios up to 1000.

Moreover, the mixture equation of state is not restricted to a system involving only a liquid and its vapour. Arbitrary EOS may be combined following the procedure described previously. The case of a liquid and its vapour becomes a particular case. Associated EOS for liquid and vapour system under Stiffened Gas formulation have been recently derived in [34].

3.2. Basic CSF method

In [8], the authors build a technique, which allows numerical diffusion of the interface to model surface tension effects in an incompressible framework. This relies on the transformation of a surface force into a volume one. According to [8], the surface force is equivalent to

$$F_{sv} = \sigma\kappa\frac{\overrightarrow{\nabla\psi}}{[\psi]},$$

where ψ denotes a colour function used to locate the interface, κ is the local curvature, σ is the surface tension coefficient which is supposed to not depend on space variables and $[\psi]$ is the colour function jump across the interface. Moreover the function ψ fulfils few requirements: (i) ψ must remain constant in each fluid except in a very small neighbourhood of the interface; (ii) $\overrightarrow{\nabla\psi}$ must always be oriented toward the heaviest fluid; (iii) ψ must be continuously differentiable. Time evolution of function ψ is driven by its own governing equation which is part of the chosen physical model.

3.3. Extended CSF method: toward a conservative formulation of capillary effects

Surface tension contribution to energy balance has to be specified in order to extend the CSF method to compressible flows. Modelling of surface tension force as a volume one into the momentum equation is the basis of such an extension. For the reduced model the momentum equation becomes

$$\frac{\partial \rho \vec{u}}{\partial t} + \overrightarrow{\operatorname{div}}(\vec{u} \otimes \vec{u}) + \overrightarrow{\nabla P} = \sigma \kappa \frac{\overrightarrow{\nabla \psi}}{[\psi]},$$

where $\kappa = -\operatorname{div}\left(\frac{\overrightarrow{\nabla \psi}}{|\overrightarrow{\nabla \psi}|}\right)$. In our framework, the liquid volume fraction fits the necessary requirements of the colour function. Therefore, ψ is taken equal to the liquid volume fraction, α_2, i.e. $\psi = \alpha_2 = 1 - \alpha_1 = 1 - \alpha$ where α is the gas volume fraction.

Let $\mathbf{m}$ be the liquid volume fraction gradient. We note that $[\alpha] = 1$ when the interface separates pure fluids. So we get $F_{sv} = -\sigma \operatorname{div}\left(\frac{\mathbf{m}}{|\mathbf{m}|}\right)\mathbf{m}$. A divergent form of this force can be obtained [23].

Let us denote $\overline{\overline{T_\sigma}}$ the stress tensor due to surface tension: $\overline{\overline{T_\sigma}} = \sigma\left(|\mathbf{m}|\bar{\bar{I}} - \frac{\mathbf{m}\otimes\mathbf{m}}{|\mathbf{m}|}\right)$. The capillary force becomes $F_{sv} = \operatorname{div}(\overline{\overline{T_\sigma}})$. A conservative form of momentum equation is readily obtained:

$$\frac{\partial \rho \vec{u}}{\partial t} + \operatorname{div}\left(\rho \vec{u} \otimes \vec{u} + P\bar{\bar{I}} - \sigma\left(|\mathbf{m}|\bar{\bar{I}} - \frac{\mathbf{m}\otimes\mathbf{m}}{|\mathbf{m}|}\right)\right) = 0.$$

This form is well known and even used to compute incompressible flows [23].

The power of the stress tensor, $\phi_\sigma = \operatorname{div}(\overline{\overline{T_\sigma}} \cdot \vec{u})$, is the contribution of the surface tension effects in the energy balance. Therefore we speculate a form of the total energy equation as follows, where surface tension effects are considered:

$$\frac{\partial \mathscr{E}}{\partial t} + \operatorname{div}((\mathscr{E} + P)\vec{u}) = \phi_\sigma,$$

where the mixture total energy, $\mathscr{E}$, is expressed by $\mathscr{E} = \rho e + \frac{1}{2}\rho \vec{u}^2$. e is assumed to be the sum of the internal mixture energy ε and of a surface energy, ε_σ,to be determined.

By expanding $\phi_\sigma = \operatorname{div}\left(\overline{\overline{T_\sigma}} \cdot \vec{u}\right) = \operatorname{div}\left(\overline{\overline{T_\sigma}}\right).\vec{u} + \overline{\overline{T_\sigma}} : \bar{\bar{D}}$ where $\bar{\bar{D}}$ represents the deformation rate tensor defined by $\bar{\bar{D}}_{ij} = \frac{1}{2}\left(u_{i,j} + u_{j,i}\right)$ and by noting that $\overline{\overline{T_\sigma}} : \bar{\bar{D}} = \sigma|\mathbf{m}|\operatorname{div}(\vec{u}) + \sigma\frac{\mathrm{d}|\mathbf{m}|}{\mathrm{d}t}$, the energy equation becomes

$$\frac{\partial \mathscr{E}}{\partial t} + \operatorname{div}\left((\mathscr{E} + P)\vec{u}\right) = \operatorname{div}\left(\overline{\overline{T_\sigma}}\right) \cdot \vec{u} + \sigma|\mathbf{m}|\operatorname{div}\vec{u} + \sigma\frac{\mathrm{d}|\mathbf{m}|}{\mathrm{d}t}.$$

Combining the preceding equation with the mass and momentum equations we obtain

$$\frac{\mathrm{d}\varepsilon}{\mathrm{d}t} + \frac{P}{\rho}\operatorname{div}\vec{u} + \frac{\mathrm{d}\varepsilon_\sigma}{\mathrm{d}t} = \frac{1}{\rho}\left(\sigma|\mathbf{m}|\operatorname{div}\vec{u} + \sigma\frac{\mathrm{d}|\mathbf{m}|}{\mathrm{d}t}\right).$$

Assuming that mixture internal energy ε depends on ρ, Y_2, s and α, which are respectively mixture density, mass fraction of phase 2, mixture entropy, and gas volume fraction, we can write

$$\mathrm{d}\varepsilon = \left(\frac{\partial \varepsilon}{\partial s}\right)_{\rho,Y_2,\alpha}\mathrm{d}s + \left(\frac{\partial \varepsilon}{\partial Y_2}\right)_{\rho,s,\alpha}\mathrm{d}Y_2 + \left(\frac{\partial \varepsilon}{\partial \alpha}\right)_{\rho,Y_2,s}\mathrm{d}\alpha + \left(\frac{\partial \varepsilon}{\partial \rho}\right)_{s,Y_2,\alpha}\mathrm{d}\rho.$$

Moreover, ϕ_σ only depends on $\overrightarrow{\nabla\alpha}$ and $\vec{u}$ and does not affect neither entropy equation nor mass fraction ones which remain

$$\frac{\mathrm{d}s}{\mathrm{d}t} = 0 \quad \text{and} \quad \forall k,\ \frac{\mathrm{d}Y_k}{\mathrm{d}t} = 0.$$

Thus we obtain

$$\frac{\mathrm{d}\varepsilon_\sigma}{\mathrm{d}t} = \frac{\mathrm{d}}{\mathrm{d}t}\left(\sigma\frac{|\mathbf{m}|}{\rho}\right).$$

It follows that potential energy exists for surface tension effects, whose expression is

$$\varepsilon_\sigma = \sigma\frac{|\mathbf{m}|}{\rho}. \tag{11}$$

It is now easy to check that the conservative form of the total energy equation is

$$\frac{\partial(E+\sigma|\mathbf{m}|)}{\partial t} + \operatorname{div}\left((E+\sigma|\mathbf{m}|+P)\overrightarrow{u} - \sigma\left(|\mathbf{m}|\bar{\bar{I}} - \frac{\mathbf{m}\otimes\mathbf{m}}{|\mathbf{m}|}\right)\cdot\overrightarrow{u}\right) = 0,$$

where $E = \rho\varepsilon(\rho,s,\alpha) + \frac{1}{2}\rho\overrightarrow{u}^2$.

The resulting quasi-conservative formulation of the interface flow model with surface tension effects is

$$\begin{cases} \dfrac{\partial\alpha}{\partial t} + \overrightarrow{u}\cdot\overrightarrow{\nabla\alpha} = 0, \\ \dfrac{\partial\alpha_1\rho_1}{\partial t} + \operatorname{div}(\alpha_1\rho_1\overrightarrow{u}) = 0, \\ \dfrac{\partial\alpha_2\rho_2}{\partial t} + \operatorname{div}(\alpha_2\rho_2\overrightarrow{u}) = 0, \\ \dfrac{\partial\rho\overrightarrow{u}}{\partial t} + \overrightarrow{\operatorname{div}}\left(\rho\overrightarrow{u}\otimes\overrightarrow{u} + P\bar{\bar{I}} - \sigma\left(|\mathbf{m}|\bar{\bar{I}} - \frac{\mathbf{m}\otimes\mathbf{m}}{|\mathbf{m}|}\right)\right) = 0, \\ \dfrac{\partial E+\sigma|\mathbf{m}|}{\partial t} + \operatorname{div}\left((E+\sigma|\mathbf{m}|+P)\overrightarrow{u} - \sigma\left(|\mathbf{m}|\bar{\bar{I}} - \frac{\mathbf{m}\otimes\mathbf{m}}{|\mathbf{m}|}\right)\cdot\overrightarrow{u}\right) = 0, \end{cases} \tag{12}$$

where $\rho = \alpha_1\rho_1 + \alpha_2\rho_2$. It is quite interesting to note that, if we expand the energy equation, the previous quasi-conservative model can be written under the following non-conservative form:

$$\begin{cases} \dfrac{\partial\alpha}{\partial t} + \overrightarrow{u}\cdot\overrightarrow{\nabla\alpha} = 0, \\ \dfrac{\partial\alpha_k\rho_k}{\partial t} + \operatorname{div}(\alpha_k\rho_k\overrightarrow{u}) = 0 \quad \forall k\in\{1,2\}, \\ \dfrac{\partial\rho\overrightarrow{u}}{\partial t} + \overrightarrow{\operatorname{div}}(\rho\overrightarrow{u}\otimes\overrightarrow{u}) + \overrightarrow{\nabla P} = -\sigma\kappa\overrightarrow{\nabla\alpha}, \\ \dfrac{\partial E}{\partial t} + \overrightarrow{\operatorname{div}}((E+P)\overrightarrow{u}) = -\sigma\kappa\overrightarrow{u}\cdot\overrightarrow{\nabla\alpha}, \end{cases} \tag{13}$$

where $\kappa = -\operatorname{div}\dfrac{\overrightarrow{\nabla(-\alpha)}}{|\overrightarrow{\nabla\alpha}|} = \operatorname{div}\dfrac{\overrightarrow{\nabla\alpha}}{|\overrightarrow{\nabla\alpha}|}$.

3.4. The final model for compressible flows with interfaces including gravity, capillarity and viscous effects

We adopt the following model for compressible flows with interfaces including dissipative, capillary and gravity effects to compute flows with interfaces:

$$\begin{cases} \dfrac{\partial\alpha}{\partial t} + \overrightarrow{u}\cdot\overrightarrow{\nabla\alpha} = 0, \\ \dfrac{\partial\alpha_1\rho_1}{\partial t} + \operatorname{div}(\alpha_1\rho_1\overrightarrow{u}) = 0, \\ \dfrac{\partial\alpha_2\rho_2}{\partial t} + \operatorname{div}(\alpha_2\rho_2\overrightarrow{u}) = 0, \\ \dfrac{\partial\rho\overrightarrow{u}}{\partial t} + \overrightarrow{\operatorname{div}}\left(\rho\overrightarrow{u}\otimes\overrightarrow{u} + P\bar{\bar{I}} - \sigma\left(|\mathbf{m}|\bar{\bar{I}} - \frac{\mathbf{m}\otimes\mathbf{m}}{|\mathbf{m}|}\right) - \mu\bar{\bar{\tau}}\right) = \rho\overrightarrow{g}, \\ \dfrac{\partial E+\sigma|\mathbf{m}|}{\partial t} + \operatorname{div}\left((E+\sigma|\mathbf{m}|+P)\overrightarrow{u} - \sigma\left(|\mathbf{m}|\bar{\bar{I}} - \frac{\mathbf{m}\otimes\mathbf{m}}{|\mathbf{m}|}\right)\cdot\overrightarrow{u} - \mu\bar{\bar{\tau}}\cdot\overrightarrow{u}\right) = \rho\overrightarrow{g}\cdot\overrightarrow{u}, \end{cases} \tag{14}$$

where α is the gas volume fraction, ρ_k and ρ are respectively the density of phase k and the mixture density, $\overrightarrow{u}$, P, $(E + \sigma|\mathbf{m}|)$ are the mixture velocity, pressure and total energy. σ is the surface tension coefficient, $\mathbf{m}$ is the gas volume fraction gradient, μ is the mixture viscosity and $\bar{\bar{\tau}}$ is the mixture viscous stress tensor. $\overrightarrow{g}$ is the acceleration vector due to gravity.

4. Numerical method

The aim of this section is to present the various numerical procedures to solve system (14) with an Eulerian finite volume method. One of the main interesting feature of this model is that the same set of equations can be solved whatever the mesh point (mixture interfacial zone and pure fluids) by a single numerical algorithm. The model involves three main effects: (i) acoustic and convective wave propagation; (ii) capillary effects; (iii) dissipative effects due to viscosity. Thus, we develop the various ingredients and analysis for the building of an appropriate hyperbolic solver which relies on Riemann solvers and Godunov scheme. Capillary effects are directly involved in this solver. Then dissipative effects are addressed and solved in the same finite volume framework.

4.1. Mathematical analysis and Riemann solver building

The present analysis is carried out in absence of viscous effects.

Rigorously speaking conventional analysis of the corresponding system cannot be done with usual methods commonly used for hyperbolic systems analysis. Indeed, the local curvature κ whose expression is hereafter recalled $\kappa = \mathrm{div}\left(\frac{\overrightarrow{\nabla\alpha}}{|\overrightarrow{\nabla\alpha}|}\right)$ is calculated thanks to the evaluation of the divergence of the unit normal to the interface. Nevertheless, the vector $\frac{\overrightarrow{\nabla\alpha}}{|\overrightarrow{\nabla\alpha}|}$ will be considered as an independent variable. We thus assume that local curvature is frozen at a given point and a given time. The term $-\sigma\kappa\overrightarrow{\nabla\alpha}$ will be thus considered as a first order derivative term to perform a preliminary analysis on this system. Moreover, we extend here the notion of Riemann problem. Indeed, the Riemann problem is a one-dimensional notion whereas curvature is intrinsically a multi-dimensional one. However we will use this extended designation in order to evaluate some model's properties including capillary effects. Indeed, we have to check whether the model respects the Laplace law, which quantifies the pressure jump across a curved interface. Also, in order to build a corresponding "extended Riemann solver", waves speeds, Riemann invariants, shock relations and interface conditions have to be determined.

Most of the analysis is carried out with the model written under non-conservative formulation:

$$\begin{cases} \frac{\partial\alpha}{\partial t} + u\frac{\partial\alpha}{\partial x} + v\frac{\partial\alpha}{\partial y} = 0, \\ \frac{\partial\rho_1}{\partial t} + u\frac{\partial\rho_1}{\partial x} + v\frac{\partial\rho_1}{\partial y} + \rho_1\left(\frac{\partial u}{\partial x} + \frac{\partial v}{\partial y}\right) = 0, \\ \frac{\partial\rho_2}{\partial t} + u\frac{\partial\rho_2}{\partial x} + v\frac{\partial\rho_2}{\partial y} + \rho_2\left(\frac{\partial u}{\partial x} + \frac{\partial v}{\partial y}\right) = 0, \\ \frac{\partial u}{\partial t} + u\frac{\partial u}{\partial x} + v\frac{\partial u}{\partial y} + \frac{1}{\rho}\frac{\partial P}{\partial x} = -\frac{\sigma\kappa}{\rho}\frac{\partial\alpha}{\partial x}, \\ \frac{\partial v}{\partial t} + u\frac{\partial v}{\partial x} + v\frac{\partial v}{\partial y} + \frac{1}{\rho}\frac{\partial P}{\partial y} = -\frac{\sigma\kappa}{\rho}\frac{\partial\alpha}{\partial y}, \\ \frac{\partial P}{\partial t} + u\frac{\partial P}{\partial x} + v\frac{\partial P}{\partial y} + \rho c^2\left(\frac{\partial u}{\partial x} + \frac{\partial v}{\partial y}\right) = 0. \end{cases} \tag{15}$$

From this formulation it becomes obvious that the mixture entropy equation is not modified by the introduction of the capillary terms: $\mathrm{d}s/\mathrm{d}t = 0$. We can then proceed with the following analysis.

4.1.1. Jacobian matrices, eigenvalues, eigenvectors and associated approximate jumps

Model (15) is associated with the following Jacobian matrices in x- and y-directions:

$$A(U) = \frac{\partial F(U)}{\partial U} = \begin{pmatrix} u & 0 & 0 & 0 & 0 & 0 \\ 0 & u & 0 & \rho_1 & 0 & 0 \\ 0 & 0 & u & \rho_2 & 0 & 0 \\ \frac{\sigma\kappa}{\rho} & 0 & 0 & u & 0 & \frac{1}{\rho} \\ 0 & 0 & 0 & 0 & u & 0 \\ 0 & 0 & 0 & \rho c^2 & 0 & u \end{pmatrix}, \quad B(U) = \frac{\partial G(U)}{\partial U} = \begin{pmatrix} v & 0 & 0 & 0 & 0 & 0 \\ 0 & v & 0 & 0 & \rho_1 & 0 \\ 0 & 0 & v & 0 & \rho_2 & 0 \\ 0 & 0 & 0 & v & 0 & 0 \\ \frac{\sigma\kappa}{\rho} & 0 & 0 & 0 & v & \frac{1}{\rho} \\ 0 & 0 & 0 & 0 & \rho c^2 & v \end{pmatrix}.$$

Let $\overrightarrow{n}$ with $\overrightarrow{n}^t = (n_x, n_y)$ represent any vector of $\mathbb{R}^2$, then matrix A_n can be defined as $A_n = n_x \cdot A + n_y \cdot B$:

$$A_n(U) = \begin{pmatrix} u_n & 0 & 0 & 0 & 0 & 0 \\ 0 & u_n & 0 & \rho_1 n_x & \rho_1 n_y & 0 \\ 0 & 0 & u_n & \rho_2 n_x & \rho_2 n_y & 0 \\ \frac{\sigma\kappa}{\rho} n_x & 0 & 0 & u_n & 0 & \frac{n_x}{\rho} \\ \frac{\sigma\kappa}{\rho} n_y & 0 & 0 & 0 & u_n & \frac{n_y}{\rho} \\ 0 & 0 & 0 & \rho c^2 n_x & \rho c^2 n_y & u_n \end{pmatrix}.$$

The A_n eigenvalues and eigenvectors may be exhibited. First, we note that the eigenvalues of the system with capillarity and those of the system without capillarity are the same: $\lambda_1 = u_n - c$ whose order of multiplicity is 1, $\lambda_2 = u_n$ whose order is 4, and $\lambda_3 = u_n + c$ whose order is 1, where $u_n = \overrightarrow{u} \cdot \overrightarrow{n}$. As c^2 remains positive with the Stiffened Gas equation of state, we conclude that eigenvalues are real. To be sure that the addition of capillary terms does not influence the system's hyperbolicity, eigenvectors have to be determined. The right eigenvectors related to u_n are

$$r_{21} = \begin{pmatrix} 0 \\ 1 \\ 0 \\ 0 \\ 0 \\ 0 \end{pmatrix}, \quad r_{22} = \begin{pmatrix} 0 \\ 0 \\ 1 \\ 0 \\ 0 \\ 0 \end{pmatrix}, \quad r_{23} = \begin{pmatrix} 0 \\ 0 \\ 0 \\ -n_y \\ n_x \\ 0 \end{pmatrix}, \quad r_{24} = \begin{pmatrix} 1 \\ 0 \\ 0 \\ 0 \\ 0 \\ -\sigma\kappa \end{pmatrix}.$$

Eigenvectors related to $u_n + \varepsilon c$ (where $\varepsilon \in \{-1; 1\}$) are

$$r_{\varepsilon+2} = \begin{pmatrix} 0 \\ \rho_1 \\ \rho_2 \\ \varepsilon c n_x \\ \varepsilon c n_y \\ \rho c^2 \end{pmatrix}.$$

We can check the dimension of each eigenspace is equal to the order of multiplicity of each associated eigenvalue. As we have seen every eigenvalue is real, A_n is thus diagonalisable and the systems is hyperbolic.

Finally the corresponding approximate wave's jumps, β_i, can be determined. They are defined by the following formula:

$$\beta_i = l_i^t \cdot \Delta U,$$

where l_i is the left eigenvector associated to the right eigenvector r_i such that $l_k^t \cdot r_i = \delta_i^k \ \forall k$. δ_i^k represents the Kronecker symbol and $\Delta U = U_R - U_L$. The corresponding approximate wave's jumps for the present model are readily obtained:

$$\beta_1 = \frac{\Delta P}{2\rho c^2} - \frac{1}{2c}\Delta u_n + \frac{\sigma\kappa}{2\rho c^2}\Delta\alpha, \tag{16}$$

$$\beta_{21} = \Delta\rho_1 - \frac{\rho_1}{\rho c^2}\Delta P - \frac{\rho_1\sigma\kappa}{\rho c^2}\Delta\alpha, \tag{17}$$

$$\beta_{22} = \Delta\rho_2 - \frac{\rho_2}{\rho c^2}\Delta P - \frac{\rho_2\sigma\kappa}{\rho c^2}\Delta\alpha, \tag{18}$$

$$\beta_{23} = \Delta u_t, \tag{19}$$

$$\beta_{24} = \Delta\alpha, \tag{20}$$

$$\beta_3 = \frac{\Delta P}{2\rho c^2} + \frac{1}{2c}\Delta u_n + \frac{\sigma\kappa}{2\rho c^2}\Delta\alpha. \tag{21}$$

4.1.2. Laplace law

With the preceding approximate jumps it is possible to solve approximately an idealised Riemann problem where the interface has a prescribed curvature. Each wave is considered as a simple discontinuity as schematised in Fig. 2.

The right and left states on both sides of the interface are given by the following relations:

$$W_R^* = W_R - \beta_3 r_3,$$

$$W_L^* = W_L + \beta_1 r_1.$$

The pressure jump between these states is given by

$$\Delta P^* = (P_R - P_L) - (\alpha_3 + \alpha_1)\rho c^2 = \Delta P - \left(\frac{2\Delta P}{2\rho c^2} + \frac{2\sigma\kappa\Delta\alpha}{2\rho c^2}\right)\rho c^2 = \Delta P - (\Delta P + \sigma\kappa\Delta\alpha).$$

The approximate jump condition across any curved contact discontinuity when capillarity is accounted for thus reads

$$\Delta P^* = -\sigma\kappa\Delta\alpha. \tag{22}$$

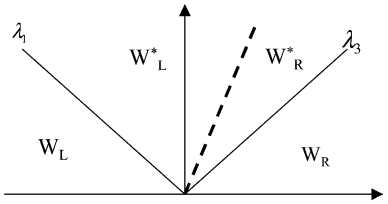

Fig. 2. Approximate Riemann problem structure used for Laplace law checking. The curved interface (dashed line) separates two media travelled by acoustic waves.

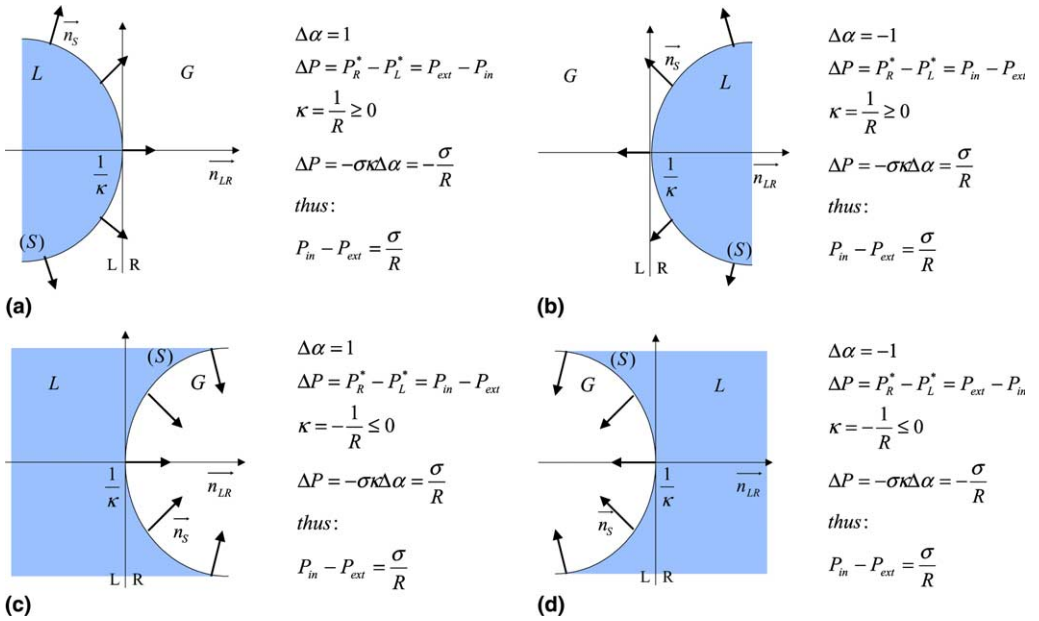

Fig. 3. The various situations that may occur at a curved interface whose curvature is κ separating a gas (G) and a liquid (L).

This last equation is fully consistent with the Laplace formula. Indeed, if we consider a curved discontinuity whose local curvature is κ, between two pure fluids ($|\Delta\alpha| = 1$) the study of the various configurations which appear at the interface location (Fig. 3) leads to the conclusion that whatever the case the Laplace law is fulfilled.

4.1.3. Riemann invariants

Riemann invariants provide jump relations for rarefaction waves and contact discontinuity. They are necessary features for the building of a Riemann solver. Riemann invariants across waves $\lambda_{\varepsilon+2} = u_n + \varepsilon c$ where $\varepsilon \in \{-1; 1\}$ can be explicitly determined in the context of the mixture Stiffened Gas equation of state since the volume fraction remains constant across these waves:

$$\Phi = \left\{ \alpha, u_t, u_n - \varepsilon \frac{2c}{\gamma - 1}, (P + P_\infty)\rho_1^{-\gamma}, (P + P_\infty)\rho_2^{-\gamma} \right\}.$$

Riemann invariants ϕ across contact discontinuity are solution of the following equation:

$$\frac{\partial\phi}{\partial\rho_1} + \frac{\partial\phi}{\partial\rho_2} - n_y \frac{\partial\phi}{\partial u} + n_x \frac{\partial\phi}{\partial v} - \sigma\kappa \frac{\partial\phi}{\partial P} + \frac{\partial\phi}{\partial\alpha} = 0. \tag{23}$$

The normal velocity obviously fulfils this last equation. The second invariant can be obtained if we assume frozen local curvature κ as it was suggested previously. Thanks to this assumption equation (23) is integrated and we obtain the last invariant across any curved contact discontinuity $\phi = P + \sigma\kappa\alpha$. Riemann invariants across contact discontinuities are thus:

$$\Phi = \{u_n, P + \sigma\kappa\alpha\}$$

which are compatible with Laplace formula.

With the ingredients provided by the present analysis the Riemann problem can be solved as detailed hereafter.

4.1.4. An exact Riemann solver

Our aim is to solve system (12) with a Godunov type scheme. In this context the various inter-cell variables and fluxes are obtained as solution of Riemann problems. The specific form of the gas volume fraction enables to build an exact Riemann solver for this model when the mixture EOS is of Stiffened Gas type. Indeed, as α remains constant along streamlines, jump condition on gas volume fraction across shock and rarefaction waves, is

$$[\alpha] = 0.$$

As Stiffened Gas EOS is used, analytical Riemann invariants have been obtained. The resulting exact Riemann solver built for the set of variables α, ρ, u, v, P and one mass fraction Y_k $(= \frac{\alpha_k \rho_k}{\rho})$, is very similar to the one for the Euler equations [21,56]. Velocity and pressure solutions of the Riemann problem for the mixture have the same expressions as those obtained for pure fluids except that in all formula γ and P_∞ must be replaced by functions of the gas volume fraction, $\gamma(\alpha)$ and $P_\infty(\alpha)$. These parameters are the mixture Stiffened Gas parameters given by the mixture EOS. Partial densities are then computed by considering the mass fractions Y_k constant across shocks or rarefaction waves too.

However some remarks are due to the presence of capillary effects. Such effects are included directly into the Riemann solvers. This is possible as long as the local curvature κ is locally frozen. Indeed, neither Rankine-Hugoniot relations and Riemann invariants are affected by the presence of capillarity. Across these waves the volume fraction is assumed constant and α space derivatives are thus cancelled. Only the pressure jump relation across contact discontinuities is modified (Eq. (22)). By replacing the pressure jump condition across contact discontinuities, $[P] = 0$, by $[P] = -\sigma\kappa[\alpha]$, we finally obtain an associated exact Riemann solver with the model for flows with interfaces including capillary effects.

4.2. Numerical approximations

The method described in this paragraph relies on a finite volume approximation with a Godunov type scheme of the capillary model given by system (12). Such method requires various ingredients as detailed hereafter.

4.2.1. Geometrical approximations

The main geometrical ingredient for numerical simulations with the capillary model is the local curvature at the cell centre and the cell boundaries. This last one is used in the Riemann solver, as previously detailed. The local curvature is considered frozen during the time step and is obtained by the following algorithm.

First we need to determine the volume fraction gradients $\overrightarrow{\nabla\alpha}$ at each cell boundaries between cell $\mathscr{C}_i$ and neighbouring cells $\mathscr{C}_j$. To do this, we extend the numerical strategy proposed in [27,53,54] in the context of viscous terms approximation to volume fraction gradient computation. This method uses two meshes. From the finite volume mesh (called primary mesh in this approach) a secondary mesh based on the primary mesh cell centres is built, as shown in Fig. 4. Then, volume fraction gradients at cell centres of the secondary mesh are obtained from the variables at cell centres of the primary mesh with the help of Green's formula, as detailed hereafter.

Let B be any primary mesh node. B is surrounded by four secondary mesh points we denote i, j, k and l (Fig. 4). These points are the tops of a quadrangle denoted by Q_B whose edges are ij, jk, kl and li respectively that we now denote by Q_{B_1}, Q_{B_2}, Q_{B_3} and Q_{B_4}. Let ϕ be any flow variable. The value of ϕ on these segments is assumed to be the arithmetic average of the values at the ends. Thus, for an (ij)-edge, we approximate

$$\phi_{ij} = \frac{\phi_i + \phi_j}{2}.$$

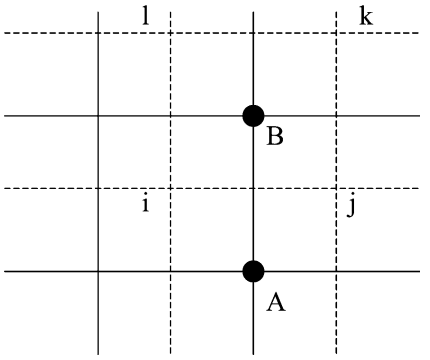

Fig. 4. Primary and secondary meshes to compute dissipative effects.

Green's formula thus provides the discrete formulation of the gradient of ϕ at the primary mesh node B:

$$\left(\overrightarrow{\nabla\phi}\right)_B = \frac{1}{\Omega_i}\sum_{Q_{B_k}} \phi_{Q_{B_k}} \overrightarrow{n}_{Q_{B_k}},$$

where $\overrightarrow{n}_{Q_{B_k}}$ is the outward normal to Q_{B_k}.

Then, the gradient at the cell boundary of the primary mesh is approximated by

$$(\overrightarrow{\nabla\phi})_{AB} = \frac{1}{2}\left((\overrightarrow{\nabla\phi})_A + (\overrightarrow{\nabla\phi})_B\right).$$

The volume fraction gradients are thus obtained by changing ϕ into α and applying the previous formulas.

Second, the cell centre mean curvature has to be determined. It is obtained by a discrete approximation of the divergence theorem:

$$\kappa_i = -\frac{1}{\Omega_i}\sum_j \mathbf{m}_{ij}\cdot\overrightarrow{n}_{ij} l_{ij}, \tag{24}$$

where Ω_i represents the volume of cell $\mathscr{C}_i$, and

$$\mathbf{m}_{ij} = \begin{cases} \dfrac{\overrightarrow{\nabla\alpha}_{ij}}{\left|\overrightarrow{\nabla\alpha}_{ij}\right|} & \text{if } |\overrightarrow{\nabla\alpha}_{ij}| \neq 0, \\ \overrightarrow{0} & \text{otherwise.} \end{cases}$$

Last, the cell boundary curvature is approximated by $\kappa_{ij} = \frac{\kappa_i+\kappa_j}{2}$.

It is worth to mention that the preceding geometrical computations cannot be done from the initial conditions where the volume fraction is discontinuous. To circumvent this difficulty a simple regularisation procedure is adopted. During the 3 first time steps the curvature is set to zero everywhere and a diffusive Riemann solver (Rusanov or HLL) is used instead of the one described previously. Such procedure smears the interfaces over 2 or 3 points and enables the computation of the various geometrical approximations described previously. After the 3 first time steps, the exact Riemann solver is used.

4.2.2. Hyperbolic operator

The hyperbolic operator consists in the numerical approximation of a quasi-conservative system: a non-conservative equation regarding the gas volume fraction, α, is present. Moreover, the model involves non-conventional fluxes. The adopted numerical strategy is detailed hereafter.

Advection scheme for the gas volume fraction

Up to our knowledge, there is no strong fundamental basis to build an appropriate numerical scheme for the gas volume fraction equation. Nevertheless, in [1,45] the authors propose a criterion which must be fulfilled by the numerical scheme in order to compute flows with interfaces:

"*If an interface evolves under uniform pressure and velocity conditions, pressure and velocity must remain uniform during time evolution*"

That recommendation may be used as a guide to derive an appropriate numerical scheme. Combining mass, momentum and energy equations, we find a result similar to the one obtained in [1,45]:

$$\alpha_i^{n+1} = \alpha_i^n - \frac{\Delta t}{\Delta x} u_i^n \left(\alpha^*_{i+\frac{1}{2}} - \alpha^*_{i-\frac{1}{2}} \right).$$

As noticed in [38,2], such approximation is a particular case of the Godunov advection scheme:

$$\alpha_i^{n+1} = \alpha_i^n - \frac{\Delta t}{\Delta x} \left((\alpha u)^*_{i+\frac{1}{2}} - (\alpha u)^*_{i-\frac{1}{2}} - \alpha_i^n \left(u^*_{i+\frac{1}{2}} - u^*_{i-\frac{1}{2}} \right) \right).$$

This scheme has shown a better convergence for interface problems than the previous one [48]. Thus, the Godunov scheme is retained in the present study. Its multi-dimensional extension reads

$$\alpha_i^{n+1} = \alpha_i^n - \frac{\Delta t}{\Omega_i} \sum_j \left(\alpha^*_{ij} - \alpha_i^n \right) \overrightarrow{u}^*_{ij} \cdot \overrightarrow{n}_{ij} l_{ij}, \tag{25}$$

where Δt denotes the time step and the variables with an asterisk are solution of the Riemann problem described previously and solved at the cell boundary ij.

One of the features of these advection schemes, combined with the conservative scheme used for the mass equations presented hereafter, is that the pure phase densities ρ_k are extended across the interface. Such property is responsible for the correct computation of temperature on both sides of the interface, as well as the ability to deal with more complex EOS than the Stiffened Gas one.

Treatment of the conservative part

In order to deal with the acoustic/convective part of the system the Godunov scheme for hyperbolic conservation laws is adopted. Let us define the conservative vector variable $W^t = (\alpha_k \rho_k, \rho \overrightarrow{u}, \mathscr{E})$ and associated fluxes

$$\mathscr{F}(W) = \begin{bmatrix} \alpha_k \rho_k \overrightarrow{u} \\ \rho \overrightarrow{u} \otimes \overrightarrow{u} + P\bar{\bar{I}} - \sigma \left(|\mathbf{m}| \bar{\bar{I}} - \frac{\mathbf{m} \otimes \mathbf{m}}{|\mathbf{m}|} \right) \\ (\mathscr{E} + P) \overrightarrow{u} - \sigma \left(|\mathbf{m}| \bar{\bar{I}} - \frac{\mathbf{m} \otimes \mathbf{m}}{|\mathbf{m}|} \right) \cdot \overrightarrow{u} \end{bmatrix},$$

where $\mathscr{E} = \rho e + \frac{1}{2} \rho \overrightarrow{u}^2$. e is the sum of the internal mixture energy ε and the surface energy $\varepsilon_\sigma = \sigma \frac{|\mathbf{m}|}{\rho}$. $\mathbf{m}$ represents the volume fraction gradient ($\mathbf{m} = \overrightarrow{\nabla \alpha}$). The dissipative and gravity effects have been omitted from system (14) for the sake of clarity. Thanks to this formulation, the conservative part of the capillary model is updated by

$$W_i^{n+1} = W_i^n - \frac{\Delta t}{\Omega_i} \sum_j \mathscr{F}^*_{ij} \cdot \overrightarrow{n}_{ij} l_{ij},$$

where $\mathscr{F}^*_{ij}$ denotes the flux $\mathscr{F}(W)$ computed with the Riemann problem solution W^*_{ij} obtained with the exact solver presented previously. The Riemann problem is solved along the cell boundary normal. Such projection is achieved with a rotation matrix and its inverse. Associated details are quite conventional with

finite volume methods for hyperbolic conservation laws. They are detailed in [56, pp. 543–549]. We prefer to detail a little more the capillary fluxes approximation.

Compared to a conventional Euler solver, two extra fluxes are present, in the momentum and energy equations:

$$F_\sigma = \mathrm{div}\left(\overline{\overline{T_\sigma}}\right),$$

$$\phi_\sigma = \mathrm{div}\left(\overline{\overline{T_\sigma}} \cdot \vec{u}\right),$$

where the capillary stress tensor $\overline{\overline{T_\sigma}}$ has been detailed in the modelling section.

Their numerical approximation is obtained as follows:

$$F_{\sigma_i} = \frac{\sigma}{\Omega_i} \sum_j \left(|\mathbf{m}|_{ij} \vec{n}_{ij} - \frac{\mathbf{m}_{ij} \cdot \vec{n}_{ij}}{|\mathbf{m}|_{ij}} \mathbf{m}_{ij} \right) l_{ij}, \tag{26}$$

$$\phi_{\sigma_i} = \frac{\sigma}{\Omega_i} \sum_j \left(|\mathbf{m}|_{ij} \vec{n}_{ij} \cdot \vec{u}^*_{ij} - \frac{\mathbf{m}_{ij} \cdot \vec{n}_{ij}}{|\mathbf{m}|_{ij}} \mathbf{m}_{ij} \cdot \vec{u}^*_{ij} \right) l_{ij}, \tag{27}$$

where Ω_i is the area of $\mathscr{C}_i$, $\vec{n}_{ij}$ is the normal to the cell boundary between $\mathscr{C}_i$ and $\mathscr{C}_j$, l_{ij} is the cell boundary length and $\mathbf{m}_{ij}$ is the gas volume fraction gradient at the cell boundary.

Another feature, specific to the present model, has to be noticed. At the end of each computational time step, the pressure has to be computed. In order to use the mixture equation of state (10) the mixture internal energy ε has to be extracted from the total energy:

$$\mathscr{E} = \rho\varepsilon + \frac{1}{2}\rho \vec{u}^2 + \sigma|\overrightarrow{\nabla\alpha}|.$$

As the volume fraction has been updated by the advection scheme (25), there is no difficulty to compute the surface energy from a cell center volume gradient approximation. The following one has been retained:

$$(\overrightarrow{\nabla\alpha})_i = \frac{1}{\Omega_i} \sum_j \alpha_{ij} \vec{n}_{ij} l_{ij}, \tag{28}$$

where $\alpha_{ij} = (\alpha_i + \alpha_j)/2$.

One can thus deduce the mixture internal energy for each cell $\mathscr{C}_i$. The volume fraction gradients are now frozen for the entire time step t^{n+1}.

The hyperbolic solver extends to second order, in order to sharpen gradients and in particular the interface. Such extension is done without difficulty on the basis of the MUSCL strategy with flux limiters. The details are given in the same book as previously recommended [56, pp. 470–476].

4.2.3. Wetting wall boundary conditions

Wall presence has a particular importance with capillary effects: rise of a liquid surface in a capillary tube due to surface tension is a good example of the phenomenon we want to take into account. Such effects are accounted for by the term $\vartheta = (\mathbf{m}_{ij} \cdot \vec{n}_{ij})/|\mathbf{m}_{ij}|$ which has a specific value for any given liquid and wall material. ϑ is the cosinus of the contact angle at the wall:

$$\vartheta = \frac{\mathbf{m}_{ij} \cdot \vec{n}_{ij}}{|\mathbf{m}|_{ij}} = \cos\theta_{\mathrm{eq}}.$$

The contact angle θ_{eq} is an experimental data well documented in the literature, and available for most liquid and solid surfaces.

As we have just seen, the wall proximity influences the topology of the contact line. So orientation of the interface and thus of the gas volume fraction gradients $\mathbf{m}_{ij}$ at the wall are modified. Consequently, for any mesh point neighbouring a solid surface, the surface tension flux balance (26) has to be computed with the volume fraction gradient $\mathbf{m}_{ij}$ corresponding to the prescribed contact angle.

4.2.4. Viscous effects

The modelling of viscous effects relies on the definition of a stress tensor and a mixture dynamic viscosity, μ, whose expressions are recalled hereafter:

$$\mu = \sum_{k=1}^{d} \alpha_k \mu_k \quad \text{and} \quad \bar{\bar{\tau}} = -\frac{2}{3}\mathrm{div}(\vec{u})\bar{\bar{I}} + 2 \cdot \bar{\bar{D}}.$$

Local contributions of viscous stresses to flux balances on momentum and total energy are

$$F_\mu = \mathrm{div}(\mu\bar{\bar{\tau}}), \tag{29}$$

$$\phi_\mu = \mathrm{div}(\mu\bar{\bar{\tau}} \cdot \vec{u}), \tag{30}$$

where F_μ and ϕ_μ are to be solved by suitable approximations. These terms being of divergence form, their numerical approximation over the computational cell reads

$$\begin{cases} F_{\mu_i} = \frac{1}{\Omega_i} \sum\limits_j \mu_{ij} \bar{\bar{\tau}}_{ij} . \vec{n}_{ij} l_{ij}, \\ \phi_{\mu_i} = \frac{1}{\Omega_i} \sum\limits_j \mu_{ij} (\bar{\bar{\tau}}_{ij} \cdot \vec{u}_{ij}) . \vec{n}_{ij} l_{ij}. \end{cases} \tag{31}$$

At every cell boundary the various variables appearing in these formulas have to be determined, in particular velocity gradients. To do this, the numerical strategy proposed in [27,53,54] is here also adopted. Indeed, by replacing ϕ in the formulas recalled in Section 4.2.1 by any of the velocity vector components, the velocity gradients at the cell boundaries are obtained. Then there is no difficulty to compute the viscous stress tensor and consequently viscous fluxes. We notice that the determination of $\vec{u}_{ij}$ is straightforward from the Riemann problem solution.

This method, described in details in [27] in the context of Navier–Stokes equations, is simple and second order accurate on cartesian grids. It was compared in [54] against the Blasius boundary layer solution and provided excellent agreement. When dealing with distorted meshes, other options are possible [18].

4.2.5. Virtual state for non-slipping wall boundary conditions

For a viscous flow, velocity at the wall is zero. Thus we add a non-slipping wall condition, $u_t|_w = 0$, to the conventional non-porous wall condition, $u_n|_w = 0$. Thus for any velocity vector $\vec{u}_i$ in a cell neighbouring a non-slipping wall, the associated velocity vector of the virtual cell is $-\vec{u}_i$.

A last remark ends this section. Gravity effects are accounted for by a conventional source term splitting.

5. Numerical validations and illustrations

The model and method capabilities are illustrated herein over physical problems involving surface tension, compressibility, viscous effects and gravity. Numerical tests are carried out to validate the numerical method step by step: (i) surface tension effects; (ii) dissipative ones; (iii) more complex problems, involving compressibility and the previous physical effects. Thus, several tests problems are examined: (i) Laplace pressure differential and deformed drop oscillations due to surface tension forces; (ii) drop creation under gravity effects; (iii) oscillations of a jet of viscous fluid; (iv) and bubble rise in a liquid bulk. For all these

tests, computed results are compared to reference data (analytical as well experimental) [10,12,14,15,37,60]. We then illustrate the ability of the method over test problems involving coupled effects: compressibility, viscosity and capillarity. Two examples are thus investigated: bubble explosion near a solid wall and colliding drops.

5.1. Dimensional analysis

Before going forward to these tests, a numerical difficulty has to be addressed: The explicit numerical scheme developed in the preceding sections is restricted by the CFL condition. The speed of sound in the liquid phase is very large so it may cause very small time steps. To circumvent this difficulty, we change the space scale of the physical problem by carrying out a dimensional analysis. The analysis is based on some useful dimensionless numbers. The first dimensionless number we use throughout this study is the Bond number, B_o. It compares the capillary pressure to the other possible pressure contributions. When gravity effects are of first order, the Bond number becomes:

$$B_{o1} = \frac{\rho g D^2}{\sigma},$$

where D and g respectively represent a characteristic length scale (typically the drop diameter) and the gravity acceleration, σ is the surface tension coefficient and ρ is the density. Otherwise, in low gravity environment the Bond number is based on surface tension and pressure, P:

$$B_{o2} = \frac{DP}{\sigma}.$$

The second dimensionless number we use is the Weber number, W_e, which compares surface tension effects to inertial forces:

$$W_e = \frac{\rho U^2 D}{\sigma},$$

where U is a velocity scale. The third one is the Reynolds number, R_e, which compares inertial forces to viscous ones:

$$R_e = \frac{\rho U D}{\mu},$$

where μ represents the dynamic viscosity of the fluid. In some particular cases (bubble rise in a liquid bulk for example) some extra dimensionless numbers can be useful:

(i) the Eötvös number:

$$E_{\ddot{o}} = \frac{g(\rho_l - \rho_g)D^2}{\sigma}$$

which is quite similar to the Bond number, except that the Eötvös number characterises liquid/gas flows;

(ii) the Morton number:

$$M = \frac{g\mu_l^4(\rho_l - \rho_g)}{\rho_l^2 \sigma^3}$$

which quantifies the influence of gravity and viscosity forces with respect to capillary forces.

Those dimensionless numbers are used to adjust surface tension coefficient, σ, gravity acceleration, g, dynamic viscosity, μ, and even initial velocity conditions.

5.2. Comparisons to analytical laws

5.2.1. Laplace formula

It is well known that Laplace has quantified the pressure jump across a curved interface. This pressure jump depends on the interface curvature and on the liquid–gas surface tension coefficient. In three dimensions, a generalised form of this law can be written as follows:

$$\Delta P = \sigma(\kappa_1 + \kappa_2),$$

where ΔP is the pressure jump, σ the surface tension coefficient, and κ_1 and κ_2 are the main local interface curvatures. We want to compare the numerical results to the analytical law to be sure that the present model reproduces Laplace results.

To do this, we consider a cylinder, whose radius is $R = 0.15$ m which is centred on the point (0.5 m; 0.5 m). The cylinder is filled with liquid, whose thermodynamic parameters are $\gamma_l = 2.1$ and $P_{\infty_l} = 10^7$ Pa and is surrounded by air, whose parameters are $\gamma_g = 1.4$ and $P_\infty = 0$ Pa. According to the generalised Laplace law, the predicted pressure jump is: $\Delta P = \sigma/R$ where R is the cylinder radius. The computational field is a square, whose edge is one-metre long. The computations have been performed over a various range of grids, from very coarse grids (70×70 cells) to fine ones (200×200 cells) using the conservative scheme to model surface tension effects. Fig. 5 shows the evolution of the relative error between the computed pressure jump and the theoretical one according to the number of points in each direction. The numerical pressure inside and outside the drop as well as numerical drop radius are built on the basis of an averaging procedure depending on a limit value for the gas volume fraction: we consider that the cells which

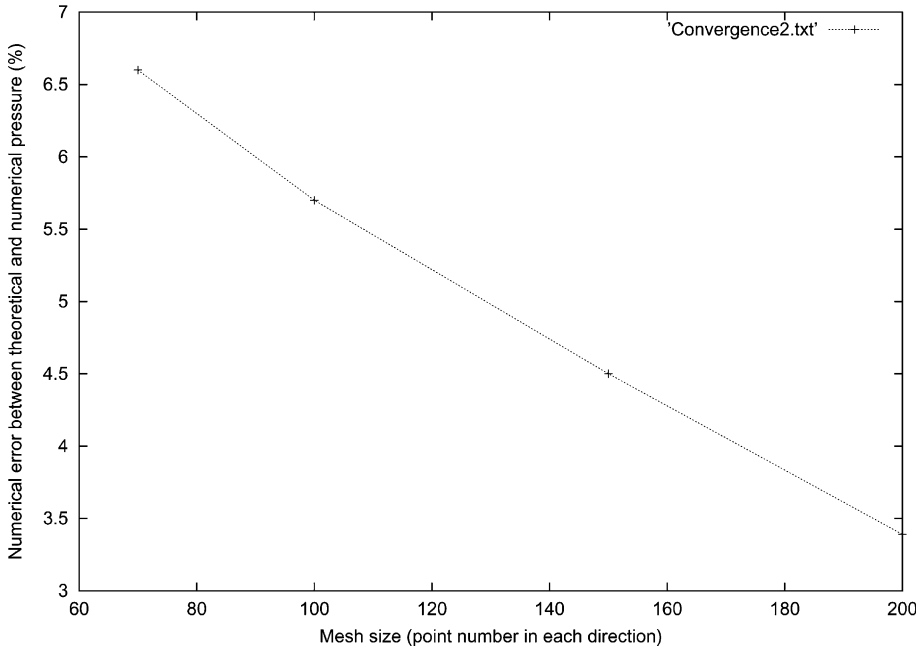

Fig. 5. Relative error of the computed pressure jump to analytical one according to the grid size.

are inside the drop are characterised by $\alpha < 0.1$. The drop is paved by telling which cells are inside the drop and those outside it. We thus find an approximate area for the cylinder and we get the corresponding radius by assuming that the drop remains circular. Fig. 5 shows that the error remains small even for coarse grids. We can also note that numerical error decreases with the cell size: the method is mesh convergent. Laplace law is well reproduced by the method.

5.2.2. Parasitic currents

Many authors have studied these phenomena [23,29] which appear at the interface. Parasitic currents are due to the competition between dissipative effects due to viscous stresses and capillarity. They are damageable because, first, they are unphysical, and second, they may lead to computational failure because of interface distortions. A miscomputation of the value of the local curvature, κ, may amplify these phenomena. Some authors [28,29] have shown that a conservative formulation of capillary effects on the momentum equation and especially on total energy equation may lead to the attenuation and even to the disappearance of parasitic currents. Aware of those drawbacks, we have performed a preliminary study of the possible appearance of those currents in our method. Our experience in the various tests shown in this article indicates that the magnitude of the parasitic currents is always very small, at least to preserve results validity when compared with experiments and to never lead to computation's failure.

But we have to investigate a little bit further before concluding that parasitic currents do not exist within our method. Indeed it has been shown that they strongly depend on the viscosity and on the Ohnesorge number ($O_h = \mu(\rho g \sigma D)^{-\frac{1}{2}}$). Both are influenced by numerical diffusion of the interfaces, which can be considered as another kind of viscosity. A proper theoretical analysis is therefore quite difficult to perform in the present framework, but is an interesting perspective.

In the following subsections, we proceed with the model validations.

5.2.3. Oscillations of an ellipsoidal drop

The behaviour of a deformed drop under surface tension effects is very useful test to check the ability of the method to manage the dynamics of these instabilities. We consider a deformed drop whose ellipsoidal shape is given by the following equation:

$$\frac{(x-0.5)^2}{0.2^2} + \frac{(y-0.5)^2}{0.12^2} = 1.$$

The computational domain is still a square, whose edge is also one-metre long. The mesh involves 111×111 cells. The time step used here is $\Delta t = 1\ \mu s$. Surrounding air is considered as an ideal gas ($\gamma_g = 1.4$, $P_{\infty_g} = 0$, $\rho_g = 1\ kg/m^3$) while the liquid thermodynamic parameters are $\gamma_l = 2.4$ and $P_{\infty_l} = 10^7$ Pa and density is $\rho_l = 100\ kg/m^3$. Fig. 6 shows the time evolution of the global average kinetic energy, which is evaluated on the entire domain. The deformed interface is initially at rest, so that kinetic energy is zero. Then interface moves because of surface tension forces. The drop gets a circular shape for an instant. But at that moment, most of the potential energy due to surface tension is converted into kinetic one so that the drop cannot stay in this equilibrium state but goes on deforming onto an ellipse. This ellipse is also a shape for which all the kinetic energy has been converted into potential energy: the velocity is close to zero everywhere but interface deformation is large. Capillary forces induce next the return to the circular shape and so on. The oscillations are thus due to the transfer of energy between its potential capillary part and kinetic one.

The physical period corresponds to two periods of the kinetic energy evolution in Fig. 6. The average evaluated radius for the equivalent circular drop is 0.15825 m. This radius is still computed by paving the drop. The numerical period of radius oscillations is then: $T = 0.0863$ s. This last value is to compare to the theoretical one. According to the modified Rayleigh formula [44], which has been extended to

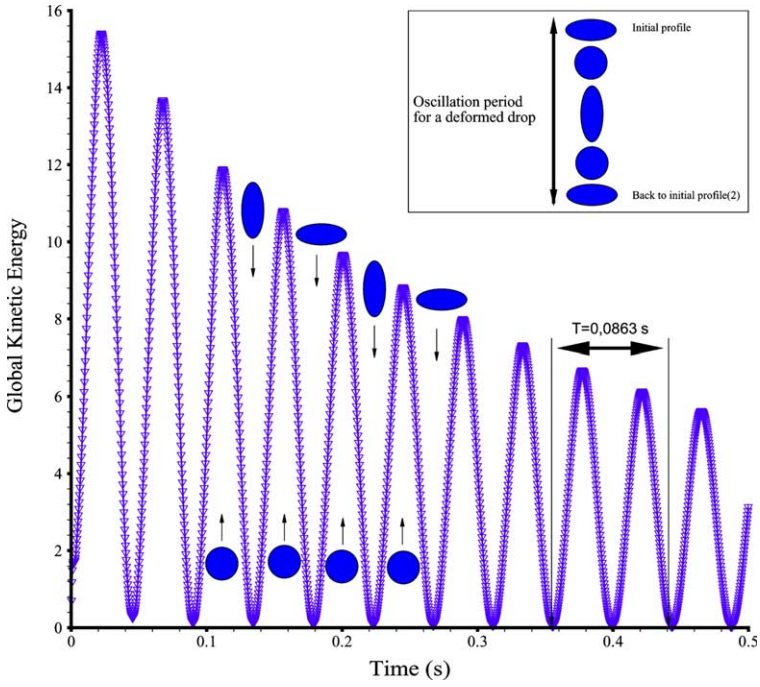

Fig. 6. Kinetic energy versus time and link with the evolution of the drop shape.

two-phase flows [17], the pulsation of a deformed liquid drop (ρ_l) that is surrounded by another fluid (ρ_g), is given by the following expression:

$$\omega^2 = (o^3 - o)\frac{\sigma}{(\rho_l + \rho_g)R^3} \quad \text{and} \quad T = \frac{2\pi}{\omega}, \tag{32}$$

where o is the oscillation mode and R is the drop radius at equilibrium state. In our case the mode of oscillation is 2. Then the theoretical value of the period is $T = 0.0878$ s. The error on the evaluation of the period is about 2%. Dynamic as well as static behaviours are thus well predicted.

5.3. Liquid break-up under gravity effects

The following test shows that interface creation is also possible with the present Eulerian method.

The physical problem we want to model is the drop formation and liquid break-up due to gravity acceleration ($g = 9.81$ m/s^2) acting on a water drop ($\sigma = 73 \times 10^{-3}$ N/m). The physical test one may imagine involves a 1.3 cm radius drop, which falls because of gravity from an upper wall. The associated Bond number is equal to 5.71.

For computational convenience, the drop radius is taken equal to 0.25 m. The drop is centered on the point (0.5 m; 1.6 m). According to the Bond number, we adjust surface tension coefficient, $\sigma = 175$ N/m, where gravity acceleration, g, is taken equal to 25 m/s^2. The vector $\vec{g}$ is oriented downward in the y-direction.

The cap is hung on the upper wetting wall thanks to surface tension effects. The contact angle at the wall boundary is taken equal to

$$\theta = 25^\circ.$$

Table 2
Fluids characteristics for liquid mass under gravity effects

	γ	P_∞ (Pa)	ρ (kg/m^3)	u (m/s)	v (m/s)	P (Pa)
Gas	1.4	0	1	0	0	10^5
Liquid	4.1	5×10^7	10^3	0	0	10^5

Initial pressure is uniform and equal to $P = 10^5$ Pa. The thermodynamic coefficients for Stiffened Gas EOS are given in Table 2.

The computational domain is 1 m wide in x-direction and 1.5 m high in y-direction. The associated mesh is composed of 200×300 computational cells. The computation is second order accurate in space and time. The calculation is performed with an imposed time step, $\Delta t = 1 \times 10^{-6}$s and over 800,000 time steps. The results presented in Fig. 7 are in good agreement with common observation. They correspond to a physical duration of 0.6 s. The spherical cap is quickly distorted due to gravity (Fig. 7(b)). It still sticks to the wall because of tension effects. The drop formation appears in Fig. 7(c) meanwhile part of the cap is still retained by the upper wall. The drop continues its formation and lengthens (Fig. 7(d)). The drop ''neck'' gets thinner and thinner until it reduces only to one point (Fig. 7(e)). At this very moment the liquid surface breaks up into several drops (a major one and several little others) which evolve freely as shown in Fig. 7(f). The mass of the drop which remains stuck to the upper wall is not sufficient to make it fall. Surface tension is thus predominant and drop still sticks to the upper wall in spite of some brief oscillations. The major drop keeps on falling down while oscillating to get back to a circular shape because of surface tension (Fig. 7(g) and (h)). The falling secondary drops even merge as Fig. 7(i) shows.

In Fig. 8, the behaviour of drop creation from both numerical (bottom) and experimental (top) results are compared. Even if computation have here been performed in a two-dimensional framework, experiment and numerical results are in good qualitative agreement. Other 2D tests have been achieved in view of quantitative comparisons. They no longer involve water but ethanol. This last fluid has been preferred because ethanol surface tension coefficient is lower than water one. Thus the liquid filament between injector and drop body is longer than with water. The filament break-up can thus be studied in more details.

The ethanol (99.99%) is injected through a pipette of 1 mm outer diameter. The created drop diameter is then 2.3 mm. The surface tension coefficient and density for ethanol are

$$\sigma_{\text{ethanol}} = 22.6 \times 10^{-3}\ \text{N/m} \quad \text{and} \quad \rho_{\text{ethanol}} = 787.9\ \text{kg/m}^3.$$

The Bond number is based on drop radius. It is equal to $B_o = 0.931$. Dimensional analysis gives an equivalent surface tension coefficient to compute a physically suitable behaviour:

$$\sigma_{\text{num}} = 332\ \text{N/m}.$$

The other fluid characteristics are summarised in Table 3. The results show a satisfactory agreement between experimental and numerical profiles in Fig. 9. As we can notice in Fig. 10 the accuracy of the numerical results is improved, when axisymmetric effects are involved: the comparison presented in Fig. 10 shows a perfect agreement between both profiles. Two different instants are presented. The result accuracy is thus not time dependent.

The various preceding tests have shown the ability of both model and numerical method to manage large interface deformations as well as dynamic interface appearance and disappearance. The computed results are in very good agreement with experiments.

5.3.1. Validation of viscous effects – 2D instabilities of a viscous jet

In the present subsection, we examine the ability of the model to compute 2D viscous flows with interfaces. The studied example consists of hydrodynamic instabilities of a highly viscous liquid jet flowing

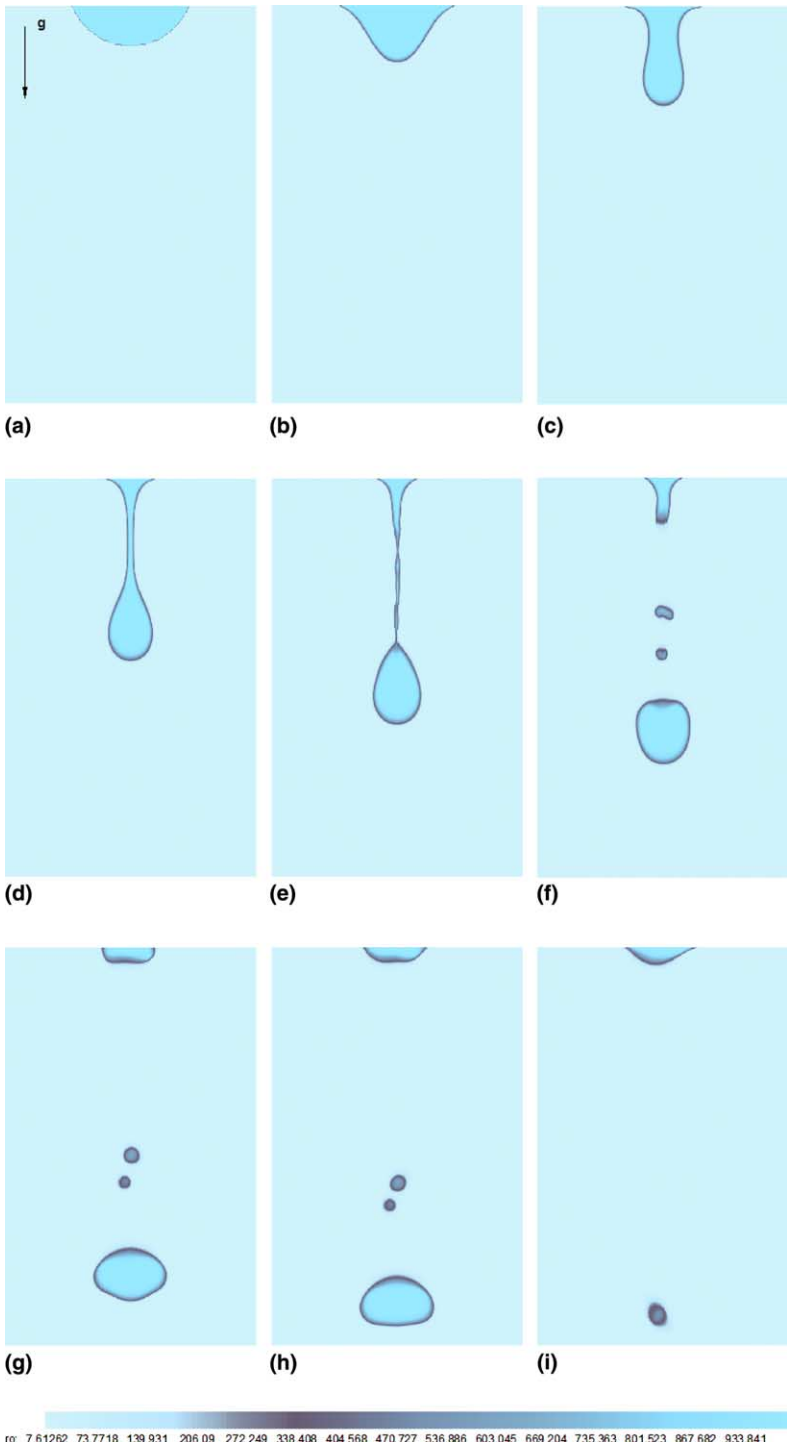

Fig. 7. Drop break-up and falling under gravity effects.

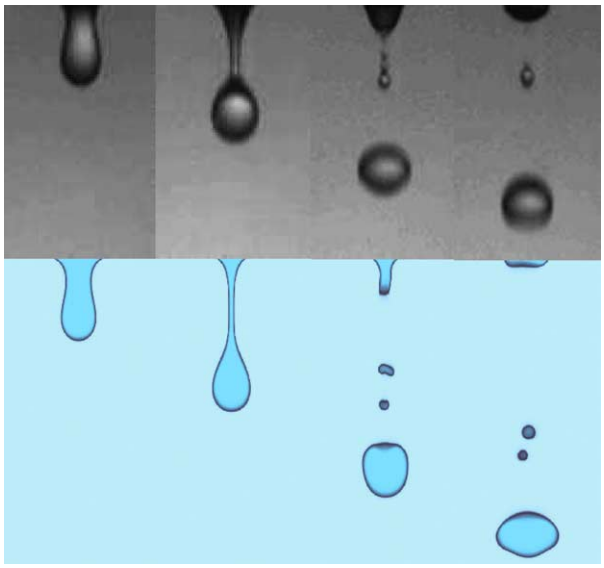

Fig. 8. Drop creation under gravity: qualitative comparison between experimental behaviour (top) – courtesy of D. Brutin (IUSTI) – and numerical 2D-behaviour (bottom).

Table 3
Fluid characteristics for the comparison with ethanol

	γ	P_∞ (Pa)	ρ (kg/m^3)	u (m/s)	v (m/s)	P (Pa)
Gas	1.4	0	1	0	0	10^5
Liquid	2.1	2×10^7	0.7879×10^3	0	0	10^5

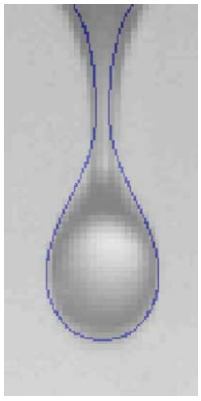

Fig. 9. Experiment and 2D computations (line). No axisymmetric effects.

under gravity, as shown in Fig. 11 by the experimental work of Cruickshank et al. [12]. This type of viscous instabilities appears under specific conditions [55]: (i) the ratio $\frac{H}{D}$ has to fulfil the following inequality, $\frac{H}{D} > 3\pi$, where D and H are respectively the injector diameter and the distance between the injector and the plate; (ii) the Reynolds number, based on the injector diameter, has to be less than 0.56.

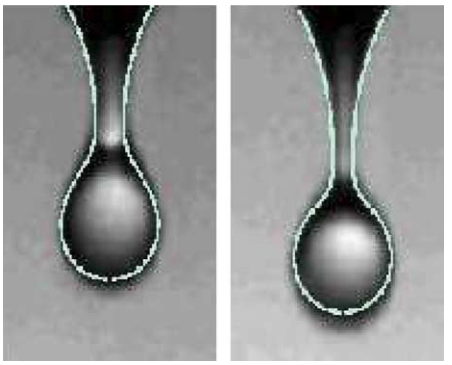

Fig. 10. Comparison between experiment (picture) and computations (line) considering axisymmetric effects.

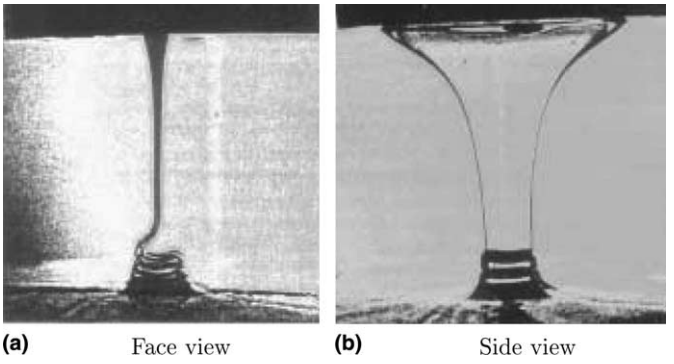

Fig. 11. Experimental study of 2D instabilities of an injected viscous jet from [12].

The computational parameters we have chosen are reported hereafter. The computational domain is a $1\text{ m} \times 1.3\text{ m}$ rectangle. The injector diameter is equal to 0.1 m while the inlet flow velocity is 1 m/s. The mesh involves 100×130 computational cells. The injector is located at the upper frontier of the domain at x-coordinate 0.5 m. The physical parameters of the injected fluid are: $\gamma_l = 5.4$, $P_{\infty_l} = 3 \times 10^7$ Pa, $\rho_l = 1800\text{ kg m}^{-3}$, and $\mu_l = 550\text{ kg m}^{-1}\text{ s}^{-1}$. The surrounding air is considered as a perfect gas whose isentropic coefficient is $\gamma_g = 1.4$. Its density is taken equal to 1 kg m^{-3}. Air dynamic viscosity equals $\mu_g = 10^{-6}\text{ kg m}^{-1}\text{ s}^{-1}$. The initial pressure is $P = 10^5$ Pa and gravity acceleration is taken equal to $g = 9.81\text{ m/s}^2$.

A second order accurate in space and time computation is performed using a fixed time step, $\Delta t = 1.5 \times 10^{-6}$ s over two-million iterations. The geometric and dynamic conditions are fulfilled so that instability regime may occur. Numerical results are shown in Fig. 12. The jet spreads into the domain while its base shrinks because of gravity (Fig. 12(c)). The jet keeps a symmetric shape until it reaches the underneath plate (Fig. 12(d)). It then oscillates (Fig. 12(f)–(h)) because of the viscous strains which induce the instabilities due to the very large dynamic viscosity ratio between liquid and gas $\left(\frac{\mu_l}{\mu_g} > 10^7\right)$. The liquid fills the domain and the free surface rises (Fig. 12(i)). Once the free surface reaches an altitude so that the geometric condition is no longer fulfilled $\left(\frac{H}{D} < 3\pi\right)$, the oscillations stop and the jet gets back to its symmetric shape. The numerical results are thus in a very good qualitative agreement with Cruickshank's experiments [12].

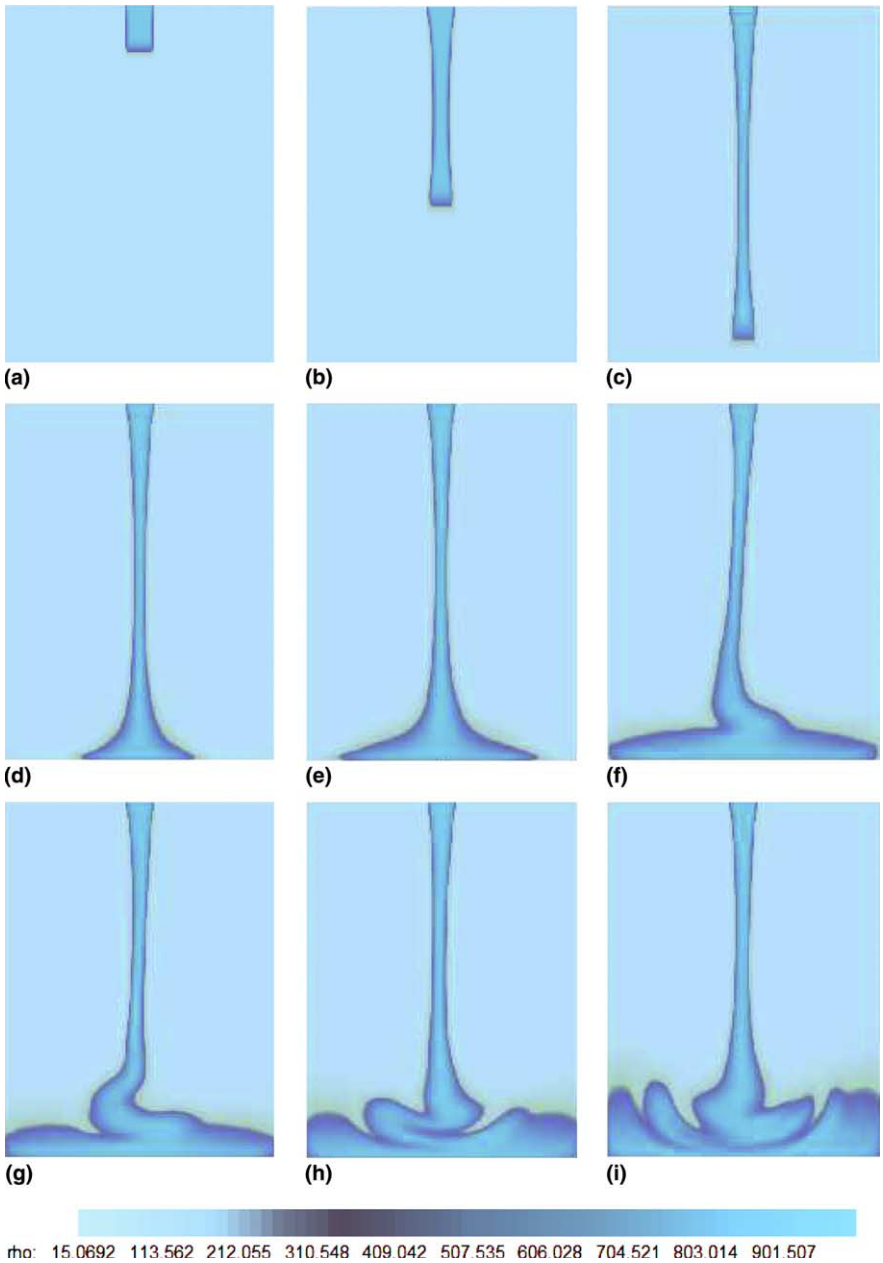

Fig. 12. 2D Oscillations of a viscous jet under gravity effects.

5.4. Coupled effects

The aim of this section is to demonstrate model's capabilities over several tests involving coupled effects with capillarity, viscosity, gravity and compressibility.

5.4.1. Rise of a gas bubble in a liquid bulk

We study hereafter the influence of surface tension, viscosity and gravity on the shape of a gas bubble rising in a liquid bulk. To deal with such a study we need extra dimensionless numbers: Eötvös ($E_{ö}$) and Morton (M) numbers.

This test is particularly interesting because many experimental results are available. For given Reynolds, Morton or Eötvös numbers the bubble shape has been reported as provided by Fig. 13. The computational domain used herein is a one-metre square involving 90×90 mesh cells. The bubble is initially deformed as an ellipse. It is centred on the point (0.5 m; 0.12 m). The lower side of the domain is a wall while absorption conditions are imposed on the other boundaries. The computation is second order accurate in space and time and the time step is $\Delta t = 5 \times 10^{-6}$ s. The thermodynamic parameters of the liquid are $\gamma_l = 2.1$ and $P_{\infty_l} = 2 \times 10^7$ Pa, its dynamic viscosity is $\mu_l = 1\ \mathrm{kg\,m^{-1}\,s^{-1}}$. Its density equals $\rho_l = 1000\ \mathrm{kg\,m^{-3}}$. The gas is a perfect one ($\gamma_g = 1.4$) whose density is 1 kg/m^3.

The computations are performed at constant Reynolds number, $R_e = \frac{\rho_l |V_l - V_g| D}{\mu_l}$, which is equal to 110. The results of two computations are shown in Fig. 14(a) and (b) where the Eötvös numbers are respectively $E_{ö} = 784$ and $E_{ö} = 130$. As geometrical bubble characteristics remain unchanged between the two tests, Eötvös number varies only because of surface tension coefficient variations. The obtained results are very similar to those of Leveque et al. [36]. Because of the surface tension, the initial ellipse tends to a circular shape, which is its least energy profile. Bubble rises to the upper side of the domain because of the buoyancy forces. Viscous stresses tend to attenuate velocity difference between liquid and gas, while capillarity guarantees the bubble cohesion. We have to note first that the higher the Eötvös number is, the less the capillary effects act. Thus, in Fig. 14(a), where $E_{ö} = 784$ surface tension forces are not strong enough for the interface to keep its cohesion: while it rises, the bubble is submitted to large distortions so that break-up tends to

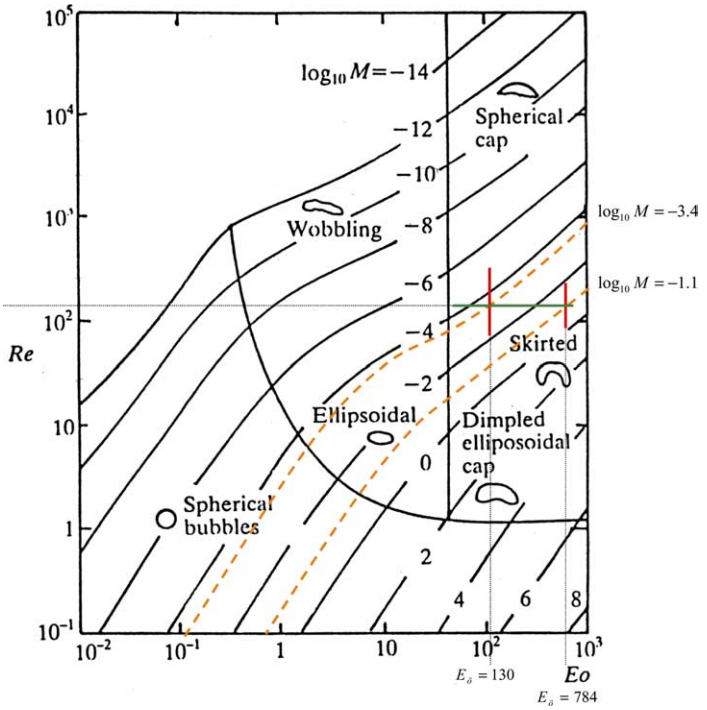

Fig. 13. Experimental bubble shape versus Reynolds, Eötvös and Morton numbers.

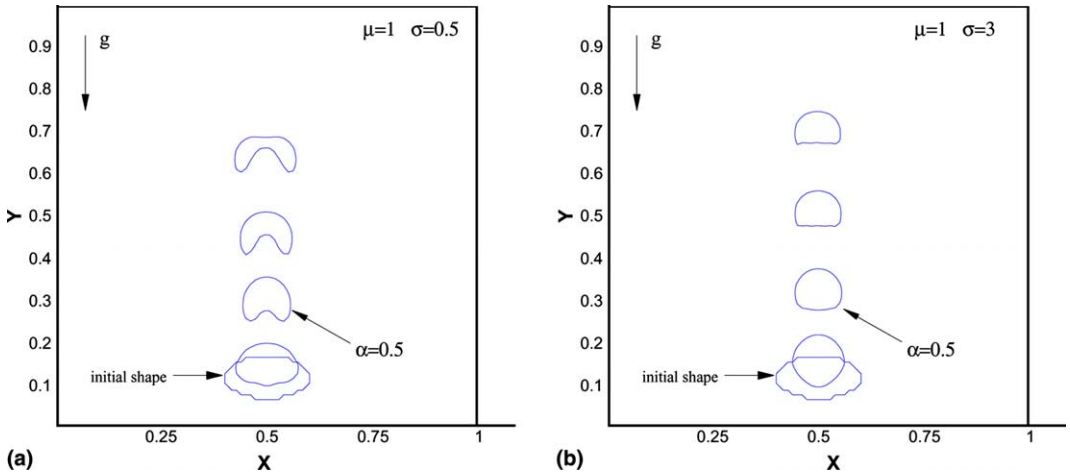

Fig. 14. Rise of a gas bubble in a viscous fluid bulk: (a) $E_{\ddot{o}} = 784,\ R_e = 110$; (b) $E_{\ddot{o}} = 130,\ R_e = 110$.

occur. In the second case, where surface tension forces are stronger and make the interface more rigid, such distortions cannot happen and the bubble shape remains quite spherical. If we locate those configurations in Fig. 13, we remark that the computed profiles are in very good agreement with the experiments.

5.4.2. Bubble explosion near a solid wall

We now deal with the simulation of gas bubble explosion and collapse near a solid wall. Such a situation appears in liquid cavitation that results in bubble creation near solid surfaces. The bubble collapse results in a high velocity liquid jet that hits the wall producing a local high pressure. When such an event is million times repeated, it may cause structure erosion and rupture. To deal with such applications, compressible effects have to be considered. Indeed, the initial pressure ratio between the gas and the liquid produces a shock wave, which propagates within the liquid. Part of the initial gas energy is transferred to the liquid by this wave. The wave also sets the liquid into motion while the bubble expands as well as the gas inside. The radial liquid flow stores kinetic energy and impulse. Compared to the gaseous phase, the liquid is very heavy. Its inertia induces an overexpansion of the gas that reaches very low pressure. The motion is thus inverted and the bubble expansion is followed by an implosion stage. As boundary conditions are not symmetrical because of the wall presence, the bubble implosion occurs with a high velocity liquid jet.

A numerical study of such a phenomenon has been carried out in [59]. In that reference, liquid is considered as incompressible. The authors used a Boundary Element Method (BEM) to compute the liquid dynamics. They so neglected the wave dynamics within the liquid, which certainly leads to an overestimation of the bubble expansion. In the present work, the liquid and gas compressibilities are inherent features of the model. The computational domain used for the computation corresponds to a two-metre edged square. the boundary conditions are absorption conditions everywhere except at the wall boundary, which is located at the lower edge, where a wetting non-sliding condition is imposed. A gas bubble, whose radius is 8 cm, is centered on the point (1 m; 0.2 m), close to the wall. The pressure inside the bubble is 3×10^6 Pa (Table 4).

Table 4
Fluids characteristics for the test related to the bubble explosion near a solid wall

	γ	P_∞ (Pa)	μ (kg/m/s)	ρ (kg/m^3)	u (m/s)	v (m/s)	P (Pa)
Gas	1.4	0	1.1×10^{-5}	10	0	0	10^5
Liquid	5	2×10^8	10^{-3}	10^3	0	0	3×10^6

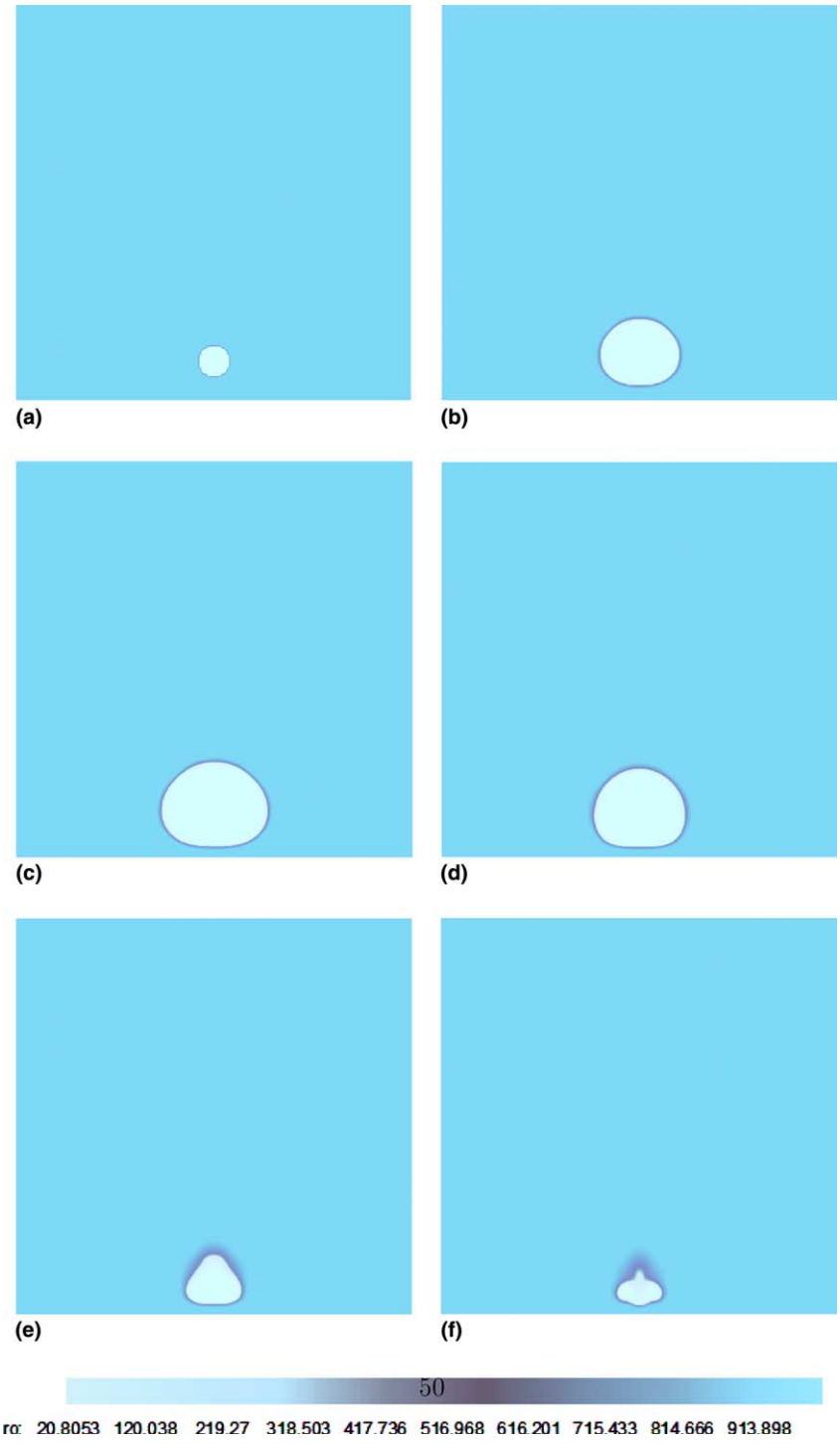

Fig. 15. Bubble explosion near a solid wall (1/2).

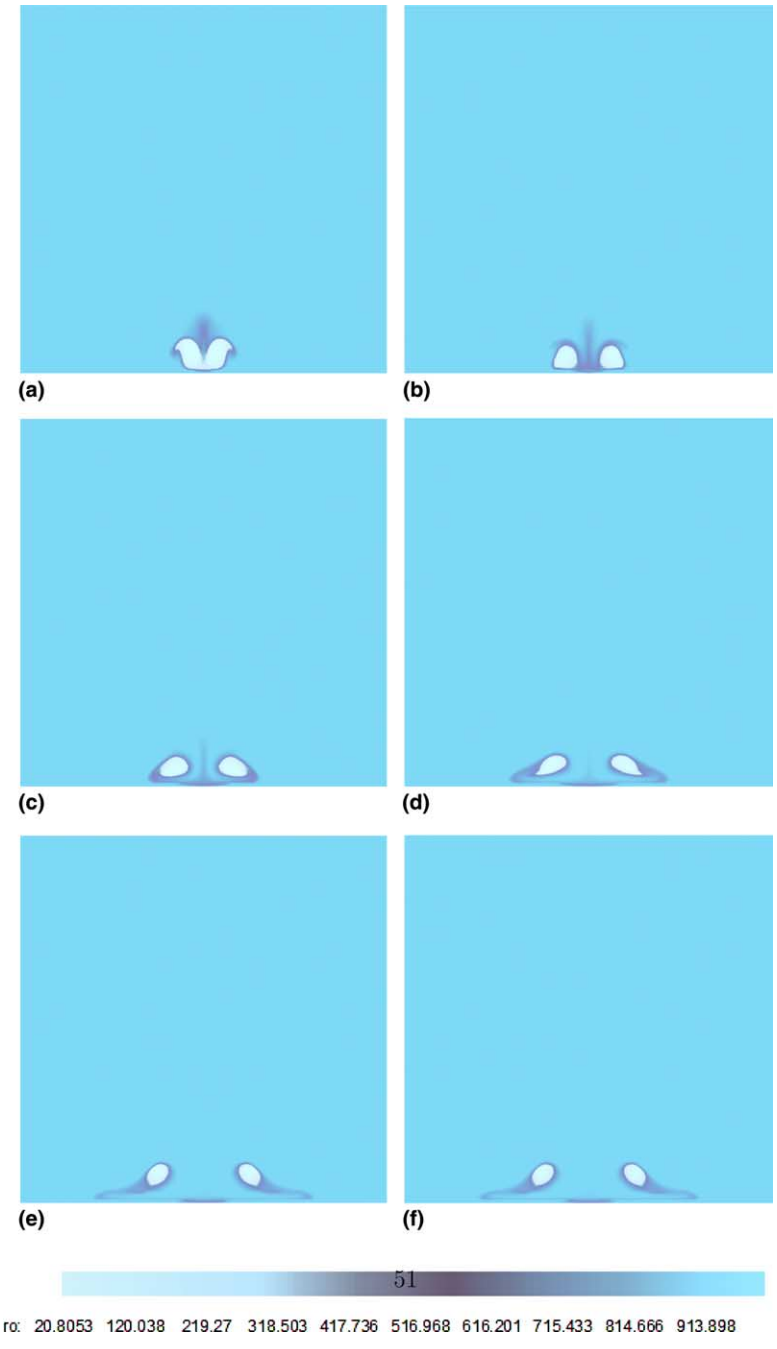

Fig. 16. Bubble explosion near a solid wall (2/2).

The dimensionless parameters for this computation are the Bond number $B_o = 0.95$ and the Morton number $M_o = 2, 5 \times 10^{-11}$. The numerical bubble corresponds to a physical 1.3 mm radius bubble. The wetting contact angle on the lower wall is $\theta_{eq} = 15°$.

Table 5
Fluids characteristics for drop colliding

	γ	P_∞ (Pa)	μ (kg/m/s)	ρ (kg/m^3)	u (m/s)	v (m/s)	P (Pa)
Gas	1.4	0	10^{-5}	1	0	0	10^5
Liquid drops	5	10^8	10^{-3}	10^3	± 5	0	10^5

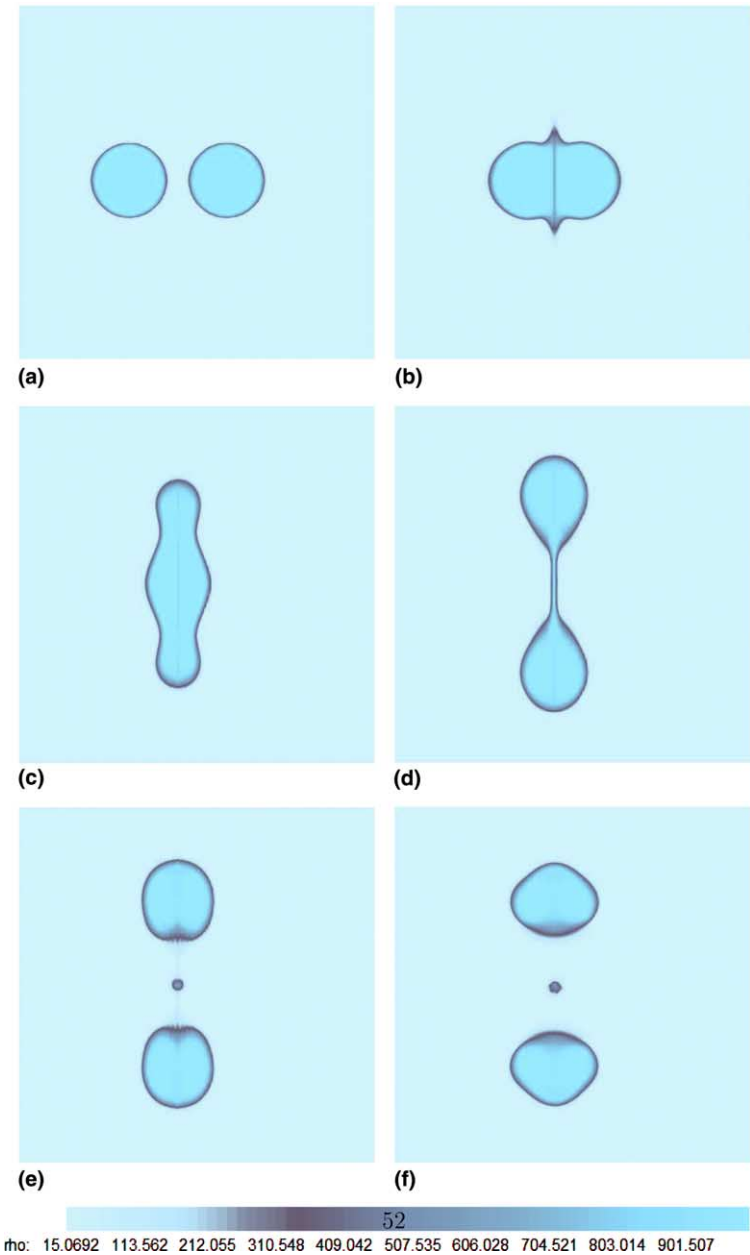

Fig. 17. Colliding liquid drops.

The computation is second order accurate in time and space over a grid involving 181×181 cells. It is performed using a fixed time step, $\Delta t = 7 \times 10^{-7}$ s, over 4×10^6 time steps. The results show the various stages of the physical phenomenon in the Figs. 15 and 16: the expansion stage is clearly visible in Fig. 15(a)–(c); then the bubble collapse appears in Fig. 15(d) and (e); jet formation stage can be clearly determined in Fig. 15(f) and in Fig. 16(a); the cylindrical bubble is then split into two sub-bubbles as it is shown in Fig. 16(b) and (c); the evolution of the vortex pair is shown up to this point. Other applications of interest involving shock waves and gas–liquid interfaces are presented in [9].

5.4.3. Colliding drops of a viscous fluid and break-up

We give here an example of numerical results obtained for the treatment of head-on collision of two liquid droplets moving at a relative velocity of 10 m/s. Capillary, viscosity, and obviously compressibility are accounted for in the computation. The computational domain is a $1\text{ m} \times 1\text{ m}$ square, which is discretised by a mesh involving 151×151 cells. Drops, whose radii are 0.1 m, are initially located at points (0.3 m; 0.5 m) and (0.6 m; 0.5 m) (Table 5). Surface tension coefficient is taken equal to $\sigma = 831$ N/m. Capillary effects are accounted for as well as viscous effects. Neither gravity nor axisymmetric effects are here considered. The computation is second order accurate. The imposed time step is $\Delta t = 1 \times 10^{-6}$ s and the calculation is performed over 800,000 time steps. Numerical results are shown in Fig. 17. On the two first graphs of Fig. 17 the two drops collide and their free surfaces merge. Forces of inertia and impact pressure expulse liquid matter away from the impact point. Capillary forces and inertia forces are here in competition. The expansion, which is visible in Fig. 17(c) induces the shrinking of the liquid filament in Fig. 17(d). The filament breaks up in Fig. 17(e) and at that moment, a secondary drop appears. The two major liquid drops then oscillate to restore a circular shape 17(f). The oscillations are smoothed and dissipated by viscous effects. At every time, the problem symmetry is preserved by the computation. This example shows that the model and the method are able to simulate drop break-up and interface oscillations in a quite complex context, where compressibility, capillarity and viscosity are taken into account.

6. Conclusion

A quasi-conservative hyperbolic compressible flow model with capillary and viscous effects has been developed for the numerical simulation of flows with material interfaces. A robust and simple algorithm has been developed for its numerical approximation.

Several tests have been performed over a wide range of physical problems involving droplet break-up, bubble coalescence, instabilities of a viscous jet, underwater explosions, rise of a gas bubble in a liquid bulk. The method is thus able to compute flows between non-miscible fluids, with high density and viscosity ratios, where large deformations of the interface occur. The method deals with dynamic appearance and disappearance of free surfaces.

Deeper analysis is to be done regarding parasitic currents. Also, model extension in the presence of heat and mass transfer is under study [35].

Acknowledgements

This work has been partially supported by Institut Français du Petrole. The authors are grateful to Veronique Henriot (IFP). They also address special thanks to David Brutin (IUSTI) for providing us experimental data, Sergey Gavrilyuk (IUSTI) for his advices regarding capillary fluids and his help all along this study, in particular regarding referee's questions and Eric Daniel (IUSTI) for his help with the numerical

approximation of viscous terms. We address also special thanks to the referees for important remarks that helped to improve the manuscript's quality.

References

[1] R. Abgrall, How to prevent pressure oscillations in multicomponent flow calculations: a quasi conservative approach, Journal of Computational Physics 125 (1996) 150–160.
[2] G. Allaire, S. Clerc, S. Kokh, A five equation model for the simulation of interfaces between compressible fluids, Journal of Computational Physics 181 (2) (2002) 577–616.
[3] C. Arcoumanis, M. Gavaises, H. Flora, H. Roth, Visualisation of cavitation in diesel engine injectors, Mechanical Industry 2 (9) (2001) 375–381.
[4] A. Chinnayya, E. Daniel, R. Saurel, Computation of detonation waves in heterogeneous energetic materials, Journal of Computational Physics 196 (2004) 490–538.
[5] C. Badock, R. Wirth, A. Fath, A. Leipertz, Investigation of cavitation in real size diesel injection nozzles, International Journal of Heat and Fluid Flow 20 (1999) 538–544.
[6] M.R. Baer, J.W. Nunziato, A Two-phase mixture theory for Deflagration to detonation transition in granular materials, International Journal of Multiphase Flows 181 (1986) 577–616.
[7] D.J. Benson, Computational methods in Lagrangian and Eulerian hydrocodes, Computer Methods in Applied Mechanics and Engineering 99 (1992) 235–394.
[8] J.U. Brackbill, D.B. Kothe, C. Zemach, A continuum method for modeling surface tension, Journal of Computational Physics 100 (1992) 335–354.
[9] N. Bremond, E. Villermaux, Bursting thin liquid films, Journal of Fluid Mechanics 524 (2005) 121–130.
[10] D. Brutin, Drop impingement on a deep liquid surface: study of a crater's sinking dynamics, CRAS Note, C.R. Mecanique 331 (2003).
[11] J.W. Cahn, J.E. Hilliard, Free energy of a nonuniform system. Part I: Interfacial free energy, Journal of Chemical Physics 28 (2) (1958) 258.
[12] J.O. Cruickshank, Low-Reynolds-number instabilities in stagnating jet flow, Journal of Fluid Mechanics 193 (1988) 111–127.
[13] D.A. Drew, Mathematical modeling of two-phase flows, Annual Review of Fluid Mechanics 15 (1983) 261–291.
[14] J. Eggers, Nonlinear dynamics and breakup of free surface flows, Review of Modern Physics 69 (3) (1997) 293–310.
[15] J. Eggers, J. Lister, H.A. Stone, Coalescence of liquid drops, Journal of Fluid Mechanics 401 (1999) 293–310.
[16] C. Farhat, F.X. Roux, An method for finite element tearing and interconnecting and its parallel solution algorithm, International Journal for Numerical Methods in Engineering 32 (1991) 1205–1227.
[17] D.E. Fyfe, E.S. Oran, M.J. Fritts, Surface tension and viscosity with Lagrangian hydrodynamics on triangular mesh, Journal of Computational Physics 30 (1988) 349–384.
[18] R. Eymard, T. Gallouet, R. Herbin, Finite Volume MethodsHandbook of Numerical Analysis, VII, North-Holland, Amsterdam, 2000.
[19] S. Gavrilyuk, R. Saurel, Mathematical and numerical modeling of two-phase compressible flows with micro-inertia, Journal of Computational Physics 175 (2002) 326–360.
[20] J. Glimm, J.W. Grove, X.L. Li, K.M. Shyue, Q. Zhang, Y. Zeng, Three dimensional front tracking, SIAM Journal of Scientific Computing 19 (1998) 703–727.
[21] S.K. Godunov, A Finite difference method for numerical computation of discontinuous solutions of the equations of fluid dynamics, Math Sb. 47 (1959) 357–393.
[22] S.K. Godunov, A. Zabrodine, M. Ivanov, A. Kraiko, G. Prokopov, Résolution Numérique Des Problèmes Multidimensionnels De La Dynamique Des Gaz, Mir, Moscow, 1979.
[23] D. Gueyffier, J. Li, A. Nadim, R. Scardovelli, S. Zaleski, Volume-of-fluid interface tracking with smoothed surface stress methods for three-dimensional flows, Journal of Computational Physics 152 (1999) 423–456.
[24] F. Harlow, A. Amsden, Fluid dynamics. Monograph LA-4700, Los Alamos National Laboratory, Los Alamos, NM. (1971).
[25] C.W. Hirt, B.D. Nichols, Volume Of Fluid (VOF) method for the dynamics of free boundaries, Journal of Computational Physics 39 (1981) 201–255.
[26] C.W. Hirt, A.A. Amsden, J.L. Cook, An arbitrary Lagrangian Eulerian computing method for all flow speeds, Journal of Computational Physics 135 (1997) 203–216.
[27] C. Hirsch, Numerical Computation of Internal and External Flows. Volume 2: Computational Methods for Inviscid and Viscous Flows, John Wiley, USA, 1988.
[28] D. Jacqmin, An energy approach to the continuum surface tension method, AIAA paper, no. 96-08058, 1997.

[29] D. Jamet, D. Torres, J.U. Brackbill, On the theory and computation of surface tension: the elimination of parasitic currents through energy conservation in the second gradient method, Journal of Computational Physics 182 (1) (2002) 262–276.
[30] D. Jamet, O. Lebaigue, N. Coutris, J.M. Delhaye, The second Gradient method for the direct numerical simulation of liquid–vapor flows with phase change, Journal of Computational Physics 169 (2) (2001) 624–651.
[31] A.K. Kapila, R. Menikoff, D.S. Stewart, Two-phase modeling of deflagration to detonation transition in granular materials: reduced equations, Physics of Fluids 13 (10) (2001) 3002–3024.
[33] S. Karni, Multicomponent flow calculations by a consistent primitive algorithm, Journal of Computational Physics 112 (1994) 31–43.
[34] O. Le Metayer, J. Massoni, R. Saurel, Elaboration des lois d'état d'un liquide et de sa vapeur pour les modèles d'écoulements diphasiques, International Journal of Thermal Sciences 43 (2003) 265–276.
[35] O. Le Metayer, J. Massoni, R. Saurel, Modelling evaporation fronts with reactive Riemann solvers, Journal of Computational Physics 205 (2) (2005) 567–610.
[36] R.J. Leveque, Z. Li, Immersed interface methods for stokes flow with elastic boundaries or surface tension, SIAM Journal on Scientific Computing 18 (3) (1997) 709–735.
[37] P. Marmottant, E. Villermaux, On spray formation, Journal of Fluid Mechanics 498 (2004) 73–111.
[38] J. Massoni, R. Saurel, B. Nkonga, R. Abgrall, Propositions de méthodes et modèles eulériens pour les problèmes á interfaces entre fluides compressibles en présence de transfert de chaleur, International Journal of Heat and Mass Transfer 45 (6) (2002) 1287–1307.
[39] W. Mulder, S. Osher, J.A. Sethian, Computing interface motion: the compressible Rayleigh–Taylor and Kelvin–Helmholtz instabilities, Journal of Computational Physics 100 (1992) 209.
[40] A. Murrone, H. Guillard, A five equation reduced model for compressible two-phase flow problems, Journal of Computational Physics 202 (2004) 664–698.
[41] S. Osher, R. Fedkiw, Level Set Methods: an overview and some recent results, Journal of Computational Physics 169 (2001) 463–502.
[42] S. Popinet, S. Zaleski, A front tracking algorithm for accurate representation of surface tension, International Journal for Numerical Methods in Fluids 30 (1999) 775–793.
[43] S. Popinet, S. Zaleski, Bubble collapse near a solid boundary: a numerical study of the influence of viscosity, Journal of Fluid Mechanics 464 (2002) 137–163.
[44] Lord Rayleigh, On the capillarity phenomena of jets, Proceedings of the Royal Society London Series A 29 (1879) 71–97.
[45] R. Saurel, R. Abgrall, A simple method for compressible multifluid flows, SIAM Journal on Scientific Computing 21 (3) (1999) 1115–1145.
[46] R. Saurel, R. Abgrall, A multiphase Godunov method for compressible multifluid and multiphase flows, Journal of Computational Physics 150 (1999) 425–467.
[47] R. Saurel, O. Le Metayer, A multiphase model for compressible flows with interfaces, shocks, detonations, waves and cavitation, Journal of Fluid Mechanics 431 (2001) 239–271.
[48] R. Saurel, S. Gavrilyuk, F. Renaud, A multiphase model with internal degrees of freedom: application to shock–bubble interaction, Journal of Fluid Mechanics 496 (2003) 283–321.
[49] K.M. Shyue, An efficient shock-capturing algorithm for compressible multicomponent problems, Journal of Computational Physics 142 (1998) 142.
[50] D.R. Scheffer, J.A. Zukas, Practical aspects of numerical simulation of dynamic events: material interfaces, International Journal of Impact Engineering 24 (5–6) (2000) 821–842.
[51] J. Sethian, Evolution, implementation and application of level set and fast marching methods for advancing fronts, Journal of Computational Physics 169 (2001) 503–555.
[52] M. Sussman, E. Fatemi, P. Smereka, S. Osher, An improved level set method for incompressible two-phase flows, Computers and Fluids 27 (5–6) (1998) 663–680.
[53] N. Thévand, E. Daniel, J.C. Loraud, On high resolution schemes for compressible viscous two-phase dilute flows, International Journal for Numerical Methods in Fluids (31) (1999) 681–702.
[54] N. Thévand, E. Daniel, Numerical study of particle behaviour in laminar shock induced boundary layer flows, Shock Waves 11 (4) (2002) 279–288.
[55] M.F. Tomé, B. Duffy, S. Mc Knee, A numerical technique for solving unsteady non-Newtonian free surface flows, Journal of Non-Newtonian Fluid Mechanics 62 (1996) 9–34.
[56] E.F. Toro, in: Presse (Ed.), Riemann Solvers and Numerical Methods for Fluid Dynamics (A Practical Introduction), Springer-Verlag, Heidelberg, Berlin, 1997.
[57] S. Vincent, J.P. Caltagirone, Efficient solving method for unsteady incompressible interfacial flow problems, International Journal for Numerical Methods in Fluids 30 (1999) 795–811.
[58] G. Wallis, in: Presse (Ed.), One-Dimensional Two-phase Flow, McGraw-Hill Company, New York, 1969.

[59] C. Wang, B.C. Khoo, An indirect boundary element method for three-dimensional explosion bubbles, Journal of Computational Physics 194 (2004) 451–480.
[60] A.M. Worthington, A Study of Splashes, Presse, Longmans Green and Company, London, 1908.
[61] S. Zaleski, J. Li, S. Succi, Two-dimensional Navier–Stokes simulation of deformation and breakup of liquid patches, Physical Review Letters 75 (2) (1995) 244–247.
[62] H.K. Zhao, S. Osher, B. Merriman, M. Kang, Level set methods: an overview and some recent results, Computer Vision and image understanding 80 (2000) 295–314.